



1 Satellite ice extent, sea surface temperature, and atmospheric 2 methane trends in the Barents and Kara seas

3 Ira Leifer¹, F. Robert Chen², Thomas McClimans³, Frank Muller Karger², Leonid Yurganov⁴

4 ¹ Bubbleology Research International, Inc., Solvang, CA, USA

5 ² University of Southern Florida, USA

6 ³ SINTEF Ocean, Trondheim, Norway

7 ⁴ University of Maryland, Baltimore, USA

8 Correspondence to: Ira Leifer (ira.leifer@bubbleology.com)

9

10 **Abstract.** Long-term (2003-2015) satellite-derived sea-ice extent, sea surface temperature (*SST*), and lower
11 tropospheric methane (CH_4) of the Barents and Kara Seas (BKS) were analyzed for statistically significant
12 anomalies and trends for 10 focus areas and on a pixel basis that were related to currents and bathymetry. Large
13 positive CH_4 anomalies were discovered around Franz Josef Land (FJL) and offshore west Novaya Zemlya in early
14 fall. Far smaller CH_4 enhancement was around Svalbard, downstream of known seabed seepage.

15 Strongest *SST* increase was southeast Barents Sea in June due to strengthening of the warm Murman Current
16 (MC) and in the south Kara Sea in September, when the cold Percey Current weakens and the MC strengthens.
17 These regions and around FJL exhibit the strongest CH_4 growth. Likely sources are CH_4 seepage from subsea
18 permafrost and hydrates and the petroleum reservoirs underlying the central and east Barents Sea and the Kara Sea.
19 The spatial pattern was poorly related to depth and better explained by shoaling. Peak CH_4 anomaly is several
20 months after peak *SST*, consistent with a several month delay between *SST* and seabed temperature. Continued MC
21 strengthening will increase heat transfer to the BKS, rendering the Barents Sea ice-free in about 15 years.

22

23 **Keywords:** Arctic, methane, sea surface temperature, ice, Barents Sea, warming, currents, emissions

24

25 Highlights:

- 26 • Warm, northwards flowing Murman Coastal Current penetrates further into the Barents and Kara seas
- 27 • Currents transport positive *SST* and drive growing methane emissions
- 28 • Shoaling provides a mechanism that allows deep-water methane to reach the atmosphere
- 29 • Franz Josef Land and the west coast of Novaya Zemlya are important, un-inventoried and growing CH_4 sources

30



31 1. Introduction

32 1.1 Changes in the Arctic Environment in the Anthropocene

33 Over recent decades, the Arctic has been experiencing amongst the fastest changes from global warming,
34 termed Arctic amplification (Manabe and Stouffer, 1980) with the Arctic Ocean warming at nearly double the rate
35 of the rest of the world's oceans (Hoegh-Guldberg and Bruno, 2010). Arctic amplification is strongly evident in the
36 progressive reduction of sea ice cover over the Arctic Ocean associated with sea surface temperature increases
37 (Comiso, 2012; Comiso et al., 2008; Graverson et al., 2008; Hoegh-Guldberg and Bruno, 2010; Overland and Wang,
38 2013; Screen and Simmonds, 2010; Stroeve et al., 2014). Data since 1948 show that Arctic Ocean and atmospheric
39 temperatures and storm frequency increased as sea ice extent and volume decreased (NRC, 2014).

40 One of the most evident, recent manifestations of Arctic change is the observed progressive decrease in sea-ice
41 extent, which underlies numerous ocean physical (NRC, 2014) and ecosystem feedbacks (Alexander et al., 2018).
42 These include heat transfer, light availability in the water column, and momentum transfer (convective and wind
43 mixing), as well as ocean heat and moisture exchange with the atmosphere. Sea ice changes affect weather and
44 overall surface albedo (NRC, 2014).

45 The Arctic has global impacts by directly affecting weather including extremes at mid-latitudes (Cohen et al.,
46 2014), by affecting global albedo and hence the earth's energy balance (NRC, 2014), and by contributing to the
47 budgets of methane (CH₄), a potent greenhouse gas with greater radiative impact on a 20 year time scale than carbon
48 dioxide (IPCC, 2007; Fig. 2.21). Since pre-industrial times, CH₄ emissions have risen by a factor of 2.5
49 (Dlugokencky et al., 2011). Inventories have high uncertainty currently (IPCC, 2013), which is greater in future
50 projections (Saunio et al., 2016), with the Arctic contributing large uncertainty. Underlying the latter are the vast
51 Arctic CH₄, CH₄ hydrates, and organic material stores trapped under permafrost both onshore (Tarnocai et al., 2009)
52 and offshore (Archer et al., 2009). Rapid warming shallow of Arctic marginal seas will degrade the integrity of
53 submerged permafrost and its sequestered CH₄ (Shakhova et al., 2017). As a result, Arctic marine CH₄ emissions are
54 being driven by the processes that are underlie this marine warming including retreat of sea ice, heat transport by
55 currents, and increased solar energy inputs that arises in part from the higher albedo associated with sea ice retreat.

56 FIGURE 1 HERE

57 Arctic amplification has implications for seabed methane (CH₄) emissions – particularly for seabed CH₄
58 currently “sequestered” beneath subsea permafrost – terrestrial permafrost inundated by rising sea level after the
59 Holocene. For example, extensive seabed CH₄ seepage is linked closely with destabilization of subsea permafrost in
60 the East Siberian Arctic Sea (Shakhova et al., 2013) and has been estimated as comparable to emissions from Arctic
61 Tundra (Shakhova et al., 2015). Warmer seabed temperatures will degrade subsea permafrost integrity further
62 (Shakhova et al., 2017), enhancing emissions (Shakhova et al., 2015); however, time scales remain uncertain.

63 The marine Arctic also is affected by changes in the terrestrial Arctic, not just climate, but also fresh water and
64 organic material inputs from rivers. Arctic soils contain 50% of the global subterranean carbon pool of which 88% is
65 estimated sequestered in permafrost (Tarnocai et al., 2009). A quarter of this 1670 Pg (1 Pg=10¹⁵g) carbon pool may
66 be mobilized into the Arctic Ocean and sub-marginal seas over the next century due to Arctic warming (Gruber et



67 al., 2004). The Arctic and sub-Arctic show strong terrestrial, high latitude, CH₄ anomalies for eastern Canada,
68 Alaska, and Western Russia (**Fig. 1**). Still, the Barents Sea, where the most rapid ice loss has occurred (Onarheim
69 and Årthun, 2017) and the Kara Sea, show the strongest anomalies by far.

70

71 **1.2. Study Motivation**

72 We hypothesize that both lower tropospheric CH₄ and primary productivity – two parameters that are amenable
73 to remote sensing – correlate with changes in the overall water column temperature more directly than to changes in
74 sea surface temperature (*SST*), another satellite remote sensing product. Satellite data are key as they allow repeat
75 observations of multiple variables on synoptic scales. In this study, we investigate atmospheric CH₄ and *SST* trends
76 to determine the relationship in the spatial distribution of Arctic Ocean tropospheric CH₄ with respect to areas that
77 become ice-free seasonally and inter-annually.

78 The largest Arctic sea ice cover reductions over the last decade have occurred in the Barents Sea, which likely
79 will be the first ice-free arctic sea. Sea ice reduction directly affects CH₄ flux to the atmosphere by no longer
80 impeding gas transfer, but also may relate to other oceanographic changes that affect regional ocean-atmospheric
81 CH₄ fluxes. Specifically, we propose that warming *SST* relates to warmer seabed temperatures and hence CH₄
82 emissions from subsea permafrost and hydrate destabilization. The relationship between CH₄ seepage and
83 atmospheric CH₄ is indirect – seabed CH₄ must be transported across the water by bubbles, diffusion, vertical
84 mixing, and advection on timescales faster than microbial oxidation timescales.

85 We investigate this question by analyzing the timing of sea ice retreat and identifying statistically significant
86 *SST* and atmospheric CH₄ trends from satellite data for 2003-2015.

87 FIGURE 2 HERE

88 The potential for this approach was revealed in a scoping study of a small area (**Supp. Table S1, Box A2**) in the
89 marginal ice zone where Barents Sea water flows into St. Anna Trough between Franz Josef Land and Novaya
90 Zemlya (**Fig. 2b, star**). For these pixels, satellite observations 2003-2015 show a correlation between CH₄ and *SST*
91 for one of two pixel populations (**Fig. 3**). Based on this result, we test our hypothesis in marginal ice zones where
92 the relationship is predicted to be strongest. Given that the oceanography, including ice, varies dramatically across
93 the Barents and Kara seas we select ten sub-areas to elucidate how trends differ across these marginal Arctic seas.
94 Sub-areas were large enough to decrease noise and small enough not to reduce trends from averaging.

95 FIGURE 3 HERE

96 **1.3 Global and Arctic Atmospheric Methane**

97 The atmospheric CH₄ concentration has been rising in recent years (Nisbet et al., 2014) and depends on the
98 balance between sources and sinks – primarily hydroxyl (OH). Several processes may explain this trend including
99 increasing Arctic emissions, wetland emissions, fossil fuel emissions, and/or decreasing losses from OH (Ghosh et
100 al., 2015; John et al., 2012; Nisbet et al., 2014; Turner et al., 2016) compensated by decreasing biomass burning
101 (Desjardins et al., 2018). The current atmospheric lifetime of CH₄ is ~8.5-9 yr (Sonnemann and Grygashvily,



102 2014; Voulgarakis et al., 2013). Rigby et al. (2017) suggest a decline in OH likely contributed to CH₄ increases
103 since 2007. Many CH₄ source estimates have a large uncertainty (IPCC, 2013; Saunois et al., 2016) with future
104 emission estimates having still higher uncertainty (Prather et al., 2012).

105 Uncertainty is particularly acute for Arctic sources. Global atmospheric CH₄ concentrations are highest in the
106 Arctic, increasing poleward (Xiong et al., 2016). Supporting this enhancement are strong Arctic CH₄ sources,
107 including seabed emissions, terrestrial riverine runoff (Shakhova et al., 2013), and atmospheric transport from
108 terrestrial sources (industrial, permafrost, wetlands, fires, etc.). Given that Arctic OH concentrations are less than at
109 lower latitudes (Liang et al., 2017), winter Arctic CH₄ lifetime is longer than in summer. Arctic OH exhibits a
110 seasonal variability that imposes an approximately 10 ppb seasonality in CH₄ concentrations (Thonat et al., 2017).
111 Future uncertainty in Arctic sources is magnified by the strong and continued projected Arctic warming (Graversen
112 et al., 2008).

113 Arctic seabed CH₄ sources include thermogenic (geological) seepage (Shakhova et al., 2013), biogenic CH₄
114 production (James et al., 2016; Reeburgh, 2007) and submerged permafrost, originally from biogenic and/or
115 thermogenic sources (Shakhova et al., 2013). Seabed emissions largely are bubbles or dissolved gas; however,
116 microbial oxidation in near seabed sediments (the microbial filter) limits the importance of dissolved seabed CH₄
117 fluxes (Reeburgh, 2007). Bubble seepage directly transports CH₄ up into the water column and potentially the sea
118 surface after losses through dissolution. Bubble seepage also indirectly transports fluid with dissolved CH₄ (Leifer
119 and Patro, 2002). The fate of dissolved seep CH₄ depends strongly on its dissolution depth (Leifer and Patro, 2002)
120 with microbial oxidation expected to remove dissolved CH₄ below the Winter Wave Mixed Layer (WWML)
121 (Rehder et al., 1999), whereas dissolved CH₄ in the WWML mostly escapes to the atmosphere. The fraction of seep
122 CH₄ that dissolves below versus within the WWML depends strongly on seabed depth, volume flux (Leifer and
123 Patro, 2002), plume synergies that include the upwelling flow (Leifer et al., 2009), and bubble surface properties
124 including the presence of impurities on the bubble surface (Leifer and Patro, 2002). Frequent Arctic storms both
125 deepen the WWML significantly and efficiently sparge dissolved CH₄ to the atmosphere (Shakhova et al., 2013).
126 Field studies and numerical modeling have documented that even for deepsea seepage (to ~1 km) seep bubbles can
127 transport some of the CH₄ to the upper water column and potentially sea surface due to plume and deepsea bubble
128 processes (MacDonald, 2011; Rehder et al., 2009; Solomon et al., 2009; Warzinski et al., 2014).

129 **1.4. Arctic Sea Surface Temperature**

130 Arctic sea surface warming arises from several factors, including the distributions of cloud cover, sea ice, ocean
131 color, upper-ocean stratification, and heat transport between the world's oceans. Sea ice significantly reduces
132 surface albedo in the Arctic summer; thus, its absence increases absorption of solar insolation by Arctic Ocean
133 waters. This may lead to a feedback wherein reduced Arctic Ocean ice cover drives greater warming and further
134 decreasing ice. For example, anomalously warm Barents Sea SST (>+2° C in 2015 relative to 1982-2010) may be
135 associated with low sea-ice cover in this region and exposure of surface waters to direct solar heating (Timmermans,
136 2016). Ocean color affects the vertical profile of absorption of solar energy with near-surface heating more likely
137 lost to the atmosphere than deeper heating. Visible solar energy is absorbed in near surface waters by both



138 phytoplankton and other suspended and dissolved organic matter (DOM) that originates in riverine discharges
139 (Stedmon et al., 2011). The colored fraction of DOM (CDOM) reduces available light across the water column,
140 suppressing photosynthesis and increasing stratification (Granskog et al., 2007).

141 Stratification plays an important role in the Barents Sea energy budget. Barents Sea water column structure is
142 modulated by winter cooling of surface waters and their convective mixing as well as brine ejection of fresh water
143 during ice formation. Winter vertical mixing extends to the seabed over large portions of the shallow (200-300 m)
144 Barents Sea. In spring, the warming of surface waters and freshwater from melting ice support water column
145 stability and stratification in the central and southern Barents Sea (Loeng, 1991). Stratification isolates deeper waters
146 from the atmosphere and prevents vertical mixing of dissolved CH₄, trapping it in deeper water (Leifer et al., 2015)
147 while also isolating it from heat exchange with the atmosphere. Coastal waters off Norway and the Murman coast
148 remain stratified year round due to terrestrial freshwater inputs. Offshore, stratification strengthens in the spring as
149 surface waters warm and ice melts (Loeng, 1991).

150 Currents drive heat exchange between the Arctic Ocean and the Atlantic and Pacific Oceans. These exchanges
151 are major drivers of Arctic Ocean spatial thermal heterogeneity with additional inputs in coastal waters from riverine
152 outflow. Atlantic currents are the major contributor of oceanic heat to the Arctic climate system on annual (Lien et
153 al., 2013) and seasonal time scales (Lien et al., 2017). These currents include the West Spitsbergen Current
154 (Piechura and Walczowski, 2009), the Bear Island Channel Current (BICC), the Murman Current (MC), and the
155 Norwegian Atlantic Current (NAC) (see Fig. 4a), which transport Atlantic Ocean heat to the Arctic through the
156 Barents Sea. The south fork of the NAC is entrained into the Norwegian Coastal Current (NCC), which is 90%
157 Atlantic water and 10% river discharge (Skagseth et al., 2008). Variability appears related to the North Atlantic
158 Oscillation (NAO) with higher Barents Sea temperatures during the NAO's positive phase (Dickson et al., 2000).
159 This transport has caused significant warming and ice retreat in this area of the Arctic Ocean (Smedsrud et al.,
160 2013). Winds modulate the volume flow of Atlantic water into the Barents Sea – stronger in winter and weaker in
161 summer (Stiansen et al., 2009; Fig. 2.3.4). Ice processes further complicate the re-distribution of heat for surface
162 Arctic Ocean waters – ice coverage insulates the water from atmospheric cooling (heat transfer to the atmosphere),
163 better preserving its heat and thereby furthering heat transport into the Arctic (Lien et al., 2017; Lien et al., 2013).
164 Sea temperature lags atmospheric temperatures by 2-3 months, peaking for the Kola area (offshore Murman, Russia)
165 between 0 and 200 m in September-October, whereas air temperature peaks in July (Stiansen et al., 2009, Figs.
166 2.3.3, 2.3.8).

167 Positive feedbacks underlie Arctic amplification. For example, sea-ice reduction increases albedo and greater
168 heat absorption in upper water layers (IPCC, 2013). There also are more complicated feedbacks. The progression of
169 warmer water into the Barents Sea drives local winds that decrease wind-advection of sea ice, with decreased sea ice
170 coverage *increasing* heat loss from the atmosphere (Lien et al., 2017).

171 1.5. Airborne and Satellite observations of Tropospheric Methane

172 Although the Arctic covers a vast territory, our knowledge of Arctic processes is highly limited both in spatial
173 coverage and seasonal coverage. This is due to high cost, logistical challenges, and the harshness of Arctic weather.



174 Satellite sensors have advantages for Arctic observations including quick revisit times and synoptic coverage (Leifer
175 et al., 2012) and can fill the significant existing temporal and spatial gaps between the few airborne field datasets.

176 *1.5.1. Airborne Measurements*

177 A few airborne campaigns have been conducted to measure Arctic atmospheric CH₄ since 2005. Given the
178 highly extensive spatial scales of the Arctic, these campaigns provide only a few summer snapshots of a highly
179 variable domain.

180 CH₄ concentration profiles over the Arctic Ocean were measured on five flights during the HIAPER Pole-to-
181 Pole Observations (HIPPO) campaign (Kort et al., 2012; Wofsy, 2011) and produced evidence of sea surface CH₄
182 emissions from the northern Chukchi and Beaufort Seas in most profiles, up to 82°N. Enhanced concentrations near
183 the surface of the Ocean were common over fractured floating ice in sample profiles collected on 2 Nov. 2009, 21
184 Nov. 2009, and 15 Apr. 2010. On 13 Jan. 2009 and 26 Mar. 2010, when the seasonally highest level of sea-ice
185 coverage occurred, CH₄ emissions were weak or non-existent. Some of the observational variability was correlated
186 with carbon monoxide (CO), indicating terrestrial origin.

187 The Carbon in Arctic Reservoirs Vulnerability Experiment (CARVE) program sought to quantify Alaskan CO₂
188 and CH₄ fluxes between the atmosphere and surface terrestrial ecosystems. Intensive aircraft campaigns with
189 ground-based observations were conducted during summer from 2012-2015 (Chang et al., 2014). No open ocean
190 measurements were made. Additional Alaskan airborne data were collected summer 2015 (Jun.-Sept.) by the
191 Atmospheric Radiation Measurements V on the North Slope of Alaska (ARM-ACME) project (38 flights, 140
192 science flight hours), with vertical profile spirals from 150 m to 3 km over Prudhoe Bay, Oliktok Point, Barrow,
193 Atqasuk, Ivotuk, and Toolik Lake. Continuous data on CO₂, CH₄, CO, and nitrous oxide, N₂O, were collected
194 (Biraud, 2016).

195 West of Svalbard, an area of known widespread seabed CH₄ seepage aligned along a north-south fault parallel
196 to the coast (Mau et al., 2017; Westbrook et al., 2008) was the focus of a field airborne campaign June–July 2014
197 (Myhre et al., 2016). Flights were conducted using the Facility for Airborne Atmospheric Measurements (FAAM) of
198 the Natural Environment Research Council (NERC, UK). The campaign measured a suite of atmospheric trace gases
199 and was coordinated with oceanographic observations. Seabed CH₄ seepage led to significantly increased seawater
200 CH₄ concentrations. However, no significant atmospheric CH₄ enhancement was observed for the region above the
201 seeps for data collected summer, 20 Jun. – 1 Aug. 2014 (Myhre et al., 2016), albeit under a period of mostly light
202 winds.

203 *1.5.2. Satellite*

204 Satellite observations provide long-term temporal context for campaign data, which are necessarily, limited in
205 time, often limited in spatial coverage, and often only occur during a specific season when weather is acceptable for
206 flight logistics. As such, satellite observations complement high spatial-resolution airborne and boat-based field
207 observations, which are infrequent and sparse at best. Remote sensing measures column gas abundance and thus is
208 independent of potential mismatches between the platform altitude and the altitude of enhanced CH₄. Airplanes may



209 not fly sufficiently low to collect data in the planetary boundary layer (PBL), which often is shallow in the marine
210 Arctic (Aliabadi et al., 2016).

211 Satellite sensors leverage CH₄ spectral features at 1.67 and 2.32 μm in the Short Wave InfraRed (SWIR) (Clark
212 et al., 2009) and around 7.28 μm in the thermal infrared (TIR) (Tratt et al., 2014). CH₄ retrievals for SWIR sensors,
213 which use passive reflective solar radiance, are challenged in the Arctic by high cloud cover, low solar zenith angle,
214 and low reflectivity for ice, snow, and water (Leifer et al. 2013). TIR sensors measure emissivity radiance, and thus
215 comparatively shorter path lengths at high latitudes relative to SWIR sensors that measure reflected sunlight. Also,
216 TIR sensors can retrieve CH₄ above low clouds, both daytime and nighttime – SWIR is only daytime and requires
217 cloud free skies. Thus, TIR sensors have significant Arctic advantages for marine CH₄ retrievals compared to SWIR
218 sensors (Leifer et al. 2013). However, whereas SWIR sensors primarily respond to near-surface CH₄, TIR retrievals
219 generally have higher sensitivity to mid-tropospheric CH₄ than to near-surface CH₄ (Xiong et al., 2013).

220 Recent SWIR satellite CH₄ sensors include the recent Scanning Imaging Absorption SpectroMeter for
221 Atmospheric CHartographyY (SCIAMACHY-ESA: 2002-2012: 100-km resolution) mapping mission (Bovensmann
222 et al., 1999) and the active, Greenhouse Orbiting Satellite (GOSAT-JAXA: 2009-: 9-km resolution) sampling
223 mission (Kuze et al., 2009). The TROPOspheric Monitoring Instrument (TROPOMI-ESA: 2017– at 7-km
224 resolution) mapping mission (Veefkind et al., 2012) returned first images in 2017. The scheduled geostationary
225 CARBOn cycle observatory (GEOCARB-NASA; at 4-km resolution) mapping mission will return hourly (daytime)
226 revisit data for North America (Rayner et al., 2014) in the early 2020s.

227 In the TIR, the AIRS (Atmospheric InfraRed Sounder) mission onboard the Earth Observation Satellite, Aqua
228 satellite (Aumann et al., 2003b) and the EuMetsat IASI-1 (InfraRed Atmospheric Sounder Interferometer) mission,
229 on the MetOp-A platform (Clerbaux et al., 2009) provide long-term CH₄ observations. Accompanying IASI-1
230 (2007-) is IASI-2 (2013-) on the currently orbiting MetOp-B meteorological satellite. The IASI satellites follow sun
231 synchronous orbits. Additionally, three IASI New Generation instruments (Crevoisier et al., 2014) are planned for
232 launch in 2021, 2028, and 2035 (IASI-NG, 2017). AIRS CH₄ profiles are retrieved from the 7.8 μm TIR channel
233 (Aumann et al., 2003b).

234 The IASI instruments are cross-track-scanning Michelson interferometers that measure in 8461 channels at 0.5
235 cm⁻¹ spectral resolution from three spectrometers spanning 645 to 2760 cm⁻¹. These spectrometers have a 2×2 array
236 of circular footprints with a nadir spatial resolution of 12 km that is 39 × 25 km at swath (2400 km) maximum
237 (Clerbaux et al., 2009). IASI-1 was launched into an 817 km-altitude polar orbit on 19 Oct. 2006, while IASI-2 was
238 launched on 17 Sept. 2012. MetOp-A and MetOp-B cross the equator at approximately 09:30 and 21:30 local time,
239 separated by approximately half an orbit, resulting in twice daily, near-global coverage with 29 day. The on-flight
240 noise-equivalent delta temperature at 280K is estimated to be well below 0.1K in the spectral range of interest to
241 CH₄ (Razavi et al., 2009). Like AIRS, IASI has a wide swath with a scan angle of ±48.3°. IASI CH₄ retrieval
242 algorithms are described by Xiong et al. (2013) and Gambacorta (2013).

243 AIRS is a grating diffraction nadir cross-track scanning spectrometer on the Aqua satellite (2002-) that is part of
244 the Earth Observation System (Aumann et al., 2003a). AIRS was launched into a 705-km-altitude polar orbit on the
245 EOS Aqua spacecraft on 4 May 2002. The satellite crosses the equator at approximately 01:30 and 13:30 local time,



246 producing near global coverage twice a day. Effective field of view after cloud clearing, as described by Suskind et
247 al. (2006), is 45 km and the spectral resolution for CH₄ is 1.5 cm⁻¹. Version 6 of AIRS Levels 2 and 3 data are
248 publicly available (AIRS, 2016) – see Xiong et al. (2010) for a description, evaluation, and validation of global CH₄
249 AIRS retrievals. Lower-troposphere (0–4 km altitude averaged) AIRS profiles (AIRS time series is longer than IASI)
250 are analyzed herein.

251 Validation is critical to any remote sensing approach and has been addressed in a number of studies for the
252 lower and mid-upper Arctic troposphere. Xiong et al. (2010) compared aircraft data taken over Poker Flat,
253 Alaska, and Surgut, Siberia with AIRS CH₄ retrieved profiles and found agreement within 1.2% with mean
254 measured CH₄ concentration between 300–500 hPa; correlation coefficients were ~0.6–0.7. A significantly wider
255 geographical coverage was achieved for IASI validation (Xiong et al., 2013) during a quasi pole-to-pole flight of the
256 National Science Foundation’s Gulfstream V aircraft (Wofsy, 2011). A bias of nearly -1.74% was found for 374–
257 477 hPa and -0.69% for 596–753 hPa. Yurganov et al. (2016) compared 5-year long IASI data for 0–4 km layer over
258 a sea area adjacent to the Zeppelin Observatory, Svalbard, Norway, at 474 m altitude, operated by the Norwegian
259 Institute for Air Research (NILU). Monthly mean values and monthly trends were in good agreement, but daily
260 excursions did not correlate. Yurganov et al. (2016) explained the latter by the observatory’s location being near the
261 top of the planetary boundary layer.

262 IASI has been used to study lower (<4 km) tropospheric CH₄. Yurganov et al. (2016) found low atmospheric
263 CH₄ anomalies in summer for 2010–2015 with annual Arctic Ocean CH₄ fluxes estimated as being ~2/3 those from
264 the terrestrial Arctic. Positive CH₄ anomalies were observed along the coasts of Norway, Novaya Zemlya, and the
265 Svalbard archipelago primarily during November–January (Yurganov and Leifer, 2016a). A breakdown of the Arctic
266 oceanic summer thermal stratification by wind-induced mixing in autumn may underlie this seasonal trend. A
267 breakdown of stratification is proposed for CH₄ emissions to the atmosphere from the North Sea, which also is
268 highly stratified in the summer and fall (Leifer et al., 2015). Additionally, Yurganov and Leifer (2016b) report
269 significant CH₄ increases during the 2015/2016 winter over the Sea of Okhotsk.

270 **2. Method and Study Design**

271 **2.1. Overview**

272 In this study, we characterize several processes by satellite observations aggregated on a monthly basis. Satellite
273 data allow repeat regional observations spanning many years. Specifically, we investigated the relationship between
274 ice-free months, sea surface temperature (*SST*), and the atmospheric CH₄ column. We concentrate on five area types:
275 (1) Arctic water affected areas; (2) combined Arctic and Norwegian Atlantic Current affected areas; (3) Barents Sea
276 Polar Front affected areas; (4) Murman Current affected areas; and (5) Norwegian Coastal Current and Murman
277 Coastal Current affected areas.

278 Specifically, satellite products for the Barents and Kara Seas are quality reviewed and then analyzed to identify
279 statistically significant trends on both a pixel basis and in focus areas relative to regional trends (**Section 2.2**). The
280 analysis uses relative trends to reduce potential retrieval biases and uncertainty. The use of focus areas allows pixel



281 aggregation to reduce the impact of a highly spatially heterogeneous signal and to reduce the effect of inter-annual
282 spatial shifts, which could appear as local temporal variations.

283 The analysis then investigates these trends in relationship to oceanographic and meteorological processes and
284 available, Barents and Kara Seas data relevant to heat transport to, within, and between the Barents and Kara Seas
285 (**Section 2.3**). This analysis investigates the importance of different processes to improve our understanding of the
286 fate of seabed methane emissions.

287 FIGURE 4 HERE

288 **2.2. Methodology**

289 *Satellite data*

290 AIRS CH₄ data (version 6) are publicly available from NASA Goddard Space Flight Center (GSFC) since 2002
291 (AIRS Science Team/Joao Texeira, 2016). CH₄ data for 2003–2015 are retrieved by the NOAA Unique Combined
292 Atmospheric Processing System (NUCAPS) algorithm, developed at NOAA/NESDIS in cooperation with Goddard
293 Space Flight Center (GSFC). Data are analyzed for open ocean areas with high vertical thermal contrast, defined
294 here as the temperature difference between the surface and altitude of 4 km (Yurganov and Leifer, 2016a; Yurganov
295 et al., 2016). CH₄ data are re-projected to a 4-km azimuthal equal area projection. The CH₄ anomaly (CH₄[']) is
296 calculated by subtraction of the values computed within each of the 10 focus areas from the average of the whole
297 Barents Sea ocean climatology. As CH₄ shows high inter-annual variability, a three-year running average is applied.

298 Ocean SST are from the Moderate Resolution Imaging Spectroradiometer (MODIS) sensor on the Aqua satellite
299 (NASA, 2015), obtained from the GSFC, Ocean Ecology Laboratory, Ocean Biology Processing Group (OEL-
300 OBPB). The 4-km, Level 3 data are re-projected to a 4-km, equal azimuthal area projection. Satellite data products
301 are cloud screened (Ackerman et al., 2010; Ackerman et al., 1998). The mapped products match the CH₄ data
302 projection.

303 First, data are quality reviewed for sea ice coverage and cloud coverage filtered for coastlines, which are from
304 the Global Self-consistent, Hierarchical, High-resolution Shoreline database (SEADAS, 2017). Shape files of sea-ice
305 monthly extent are obtained from National Snow and Ice Data Center (Fetterer et al., 2017) and are based on
306 monthly passive microwave radiometry with the Bootstrap algorithm (Comiso et al., 2008). Sea-ice fields are
307 provided on a polar stereographic grid at 25-km resolution. The number of ice-free months is derived from the
308 intersection of the monthly ice shape file for each year with the focus areas. The number of ice-free months each
309 year is tallied by the following rules: if the intersection is less than 15%, it is counted as 0 months; if coverage is
310 greater than 15% and less than 50% of the pixel, it is counted as 0.5 months. When coverage is greater than 50% in a
311 single month the pixel is counted as ice covered for the month. Ice-covered (>50%) pixels are not used in the trend
312 or the climatology calculations for SST (CH₄ retrievals are accurate over both ice and seawater).

313 *Trend analysis*

314 To estimate trends in the Barents Sea and adjacent areas, the monthly mean time series for each grid point in the
315 images covering this region are calculated. Then, a first order polynomial is calculated by a linear regression



316 analysis. These linear trends are analyzed using the Mann Kendall Test (Önöz and Bayazit, 2003) and Sen's linear
317 trend analysis (Juahir et al., 2010; Sen, 1968).

318 Visual analysis of the trends and anomaly maps of the Barents Sea were used to determine the location of 10
319 focus areas. The average trends of the 10 focus boxes are calculated from the average of all valid pixels in each
320 focus box each year for the same months.

321 2.3. Setting

322 *Oceanography and Meteorology of the Barents and Kara Seas*

323 Significant Arctic Ocean water derives from the North Atlantic, which becomes denser through cooling.
324 Additional contributions are riverine and precipitation (which decrease water density) and Pacific water from the
325 Bering Strait. Most of this water returns to the North Atlantic as part of the global thermohaline circulation (Aagaard
326 and Carmack, 1989; Carmack and McLaughlin, 2011; Yamamoto-Kawai et al., 2008).

327 The relatively shallow (230-m average depth) Barents Sea (**Fig. 4**) is characterized by a deep Arctic shelf with
328 complex bathymetry and hydrography (Loeng, 1991). The Barents Sea is bounded to the south by the northern coast
329 of Europe, to the north by two archipelagos, Svalbard and Franz Josef Land (FJL), to the east by the large north-
330 south oriented island, Novaya Zemlya, and to the west by the Norwegian Sea. In winter, the Barents Sea is partially
331 ice-covered, while it is almost ice-free in the summer (**Fig. 4b**).

332 Barents Sea physical oceanography is influenced strongly by inflows from the North Atlantic and the Arctic
333 Ocean. North Atlantic water inflows to the Norwegian Sea, forming the Norwegian Atlantic Current (NAC), one
334 track of which becomes the West Spitsbergen Current (WSC) in the Greenland Sea and the Fram Strait, before
335 bearing eastwards to the north of Svalbard into the Arctic Ocean. The remainder flows into the Barents Sea through
336 the Barents Sea Opening. Whitehead and Salzig (2001) suggested (and demonstrated in the laboratory) that remote
337 forcing of the NAC through the Barents Sea lifts the current by several hundred meters to the sill of the Bear Island
338 Channel, forcing significant anticyclonic vorticity. This drives the retrograde Bear Island Channel Current (BICC)
339 northeast along the slope of Svalbardbanken and the prograde MC along the slope of Tromsøflaket, eastward and
340 north to the east of Central Bank (Li and McClimans, 1998; Loeng, 1991). These meet east of Central and Grand
341 Banks. The resulting flow cools from contact with the atmosphere into a denser, modified Atlantic Water flow that
342 exits through the St. Anna Trough to the east of Franz Joseph Land (Gammelsrød et al., 2009). Cooling at the banks
343 also produces a dense westward underflow, depicted by the dashed line in Fig. 4a.

344 The Norwegian Coastal Current (NCC) follows the Norwegian and Murman coastlines and incorporates fresh
345 water runoff from northern Europe and Atlantic Water. The NCC is a major contributor of oceanic heat to much of
346 the southern and eastern Barents Sea and into the Kara Sea (Lien et al., 2013). The NCC cools significantly through
347 interaction with the atmosphere, whereas the western fork of the NAC (the WSC) submerges north of Svalbard
348 (location varying seasonally) under an isolating layer of colder and fresher water, better preserving its heat (Lien et
349 al., 2013). The name of the NCC changes to the Murman Coastal Current (MCC) as crosses into Russian waters.
350 Long-term (1905-) temperature data for the upper 200 m are available from a section off the Kola Peninsula (**Fig.**
351 **4a, KS, black dashed line**), which the MCC crosses (Boitsov et al., 2012). These data reveal long-term trends with



352 a cooler period from 1875-1930 and continuous warming of $\sim 0.8^{\circ}\text{C}$ since a minimum in 1970-1980 (Skagseth et al.,
353 2008). Skagseth et al. (2008) found good agreement in the Kola Section temperature trend with the Atlantic Multi-
354 decadal Oscillation (AMO) index.

355 The MCC continues eastward at the border of the White Sea until the western shores of Novaya Zemlya divert
356 the flow northward. It then continues into the Arctic Ocean through the St. Anna Trough between Franz Josef Land
357 and Novaya Zemlya (Loeng, 1991), which is the dominant outflow of the Barents Sea (Maslowski et al., 2004). A
358 fork of the MCC flows eastward into the Kara Sea through narrow and very shallow (20-50 m) straits (see **Supp.**
359 **Fig. S2** for details of Kara Sea currents).

360 The Percey Current (PC) transports cold, low saline, Arctic surface water into the Barents Sea east of Svalbard
361 (**Supp. Fig. S1**). The intersection of the Percey Current with the warmer, high saline waters of Atlantic origin in the
362 Barents Sea gives rise to the Barents Sea Polar Front (Oziel et al., 2016), whose location is controlled by seabed
363 bathymetry, i.e., it is semi-stationary (Gawarkiewicz and Plueddemann, 1995). This front is part of a unique frontal
364 system due to its combination with the seasonally ice-covered zones in the northern, central, and eastern Barents Sea
365 (Vinje and Kvambekk, 1991). As a result, this front tends to exhibit enhanced phytoplankton blooms (Fer and
366 Drinkwater, 2014) and variability (Falk-Petersen et al., 2000). The PC merges with the East Spitsbergen Current
367 (ESC) and flows up the west Spitsbergen coast, inshore of the WSC, as the Spitsbergen Coastal Current (SCC),
368 leading to the Barents Front looping around Spitsbergen (Svendsen et al., 2002).

369 Winds in the eastern Barents Sea generally circulate counterclockwise (cyclonically), from the north along
370 Novaya Zemlya in winter and spring and weakly from the south in summer and fall (Gammelsrød et al., 2009). This
371 leads to calm over the Central Bank, easterlies to the north of Franz Josef Land and from the north to the west of
372 Svalbard (Kolstad, 2008; Moore, 2013). The Barents Sea is stormy – over 125 days per year have winds above 15 m s^{-1} ,
373 which are mostly from the south (Kolstad, 2008). In spring, winds are similar, but displaced to the south. In the
374 summer, winds blow to the south over most of the Barents Sea, except from the west off Svalbard, with average
375 summer winds of $\sim 6\text{ m s}^{-1}$ (Kolstad, 2008). In the fall, winds are similar to the summer, but stronger ($\sim 8\text{-}10\text{ m s}^{-1}$)
376 and strongly northerly between Svalbard and Greenland. Decadal-averaged air temperatures on Bear Island have
377 been rising ($\sim 2.5^{\circ}\text{C}$) since 1980 (Boitsov et al., 2012), about four times larger than the global atmospheric trend over
378 the same period of $\sim 0.6^{\circ}\text{C}$ (<http://eca.knmi.nl/>).

379 Kara Sea hydrography is controlled by the freshwater outflow of the Ob and Yenisei Rivers (**Fig. 2b; Supp.**
380 **Fig. S2**), which contribute 350 and $650\text{ km}^3\text{ yr}^{-1}$, respectively (Stedmon et al., 2011), about double that of the
381 Mississippi. Sediment from these estuaries lead to the northeast Kara Sea being mostly shallow ($< 50\text{ m}$). The
382 western Kara Sea is deep (mostly $> 100\text{ m}$), descending to below 500 m in the Novaya Zemlya Trough (Polyak et al.,
383 2002). River outflows are primarily ($> 75\%$) between May and September. As a result, east Kara Sea surface waters
384 can be brackish. The inflow of modified Atlantic water from the Barents Sea supplies the deeper water in the trough.
385 Cooler surface water from the MCC, local runoff, and ice from the north flow into the NZCC, some of which returns
386 to the Barents Sea through the Kara Strait. The trough is dense and fully saline. Cooler surface water from the Arctic
387 Ocean flows south in the narrow and weak Novaya Zemlya Coastal Current (NZCC) and exits through the Kara
388 Straits. Additionally, there is a strong, submerged, cool southward flow of Arctic Ocean water along the Novaya



389 Zemlya Trough. Warmer water enters from the Barents Sea flows east through the Kara Strait and joins a slope
390 current to the north. Much of this water mixes with the southern and returns to the Barents Sea through the northern
391 Kara Strait (McClimans et al., 1999; McClimans et al., 2000). Overall, currents through the Kara Sea are largely
392 northwards, driven by river outflow. The remainder of the north current flow splits to the west and joins the cold
393 southward NZCC. Prevailing winds are mostly from the southwest for the western Kara Sea and from the south to
394 southwest in the central Kara Sea (Kubryakov et al., 2016).

395 Ten focus areas (**Fig. 4a; Table 1** for locations) were selected based on the location of Barents and Kara Seas
396 currents and ice formation dynamics to investigate the effect of the significant differences between winter and
397 summer ice coverage. These focus areas are grouped into 5 oceanographic types. The most northerly focus areas
398 (A1-A3) characterize the inflow of Arctic surface water through both gaps between the archipelagos of Svalbard and
399 Franz Josef Land and between Franz Josef Land and Novaya Zemlya. Each of these focus areas exhibits different
400 seasonal ice coverage. Another group of focus areas are west of Svalbard (A4-A6) and are influenced by the West
401 Spitsbergen Current and water from the Barents Sea. These areas also are affected by Arctic Ocean ice outflow
402 along Greenland. A focus area near Bear Island (A7) is affected by the warm, north flowing NAC and the cold,
403 southwest-flowing Percey Current and is located in a subduction area. Two focus areas (A8 and A10) were selected
404 that are influenced by the Murman Current and Arctic water from the Percey Current in the Barents Sea Polar Front
405 region (Harris et al., 1998). Finally, one focus area (A9) is situated in the coastal waters to the west of Novaya
406 Zemlya and is influenced by the MCC with strongly, seasonally varying ice coverage.

407 **3.0 Results**

408 **3.1. Barents Sea In situ**

409 In situ CH₄ measurements were made by cavity enhanced absorption spectroscopy (Los Gatos Research Inc.,
410 Mountainview, CA). Both transits followed a very similar trajectory (**Supp. Fig. S3**) and found very strong,
411 localized, CH₄ anomalies - see **Supp. Fig. S3** for full dataset. These anomalies were far from shore, indicative of
412 local (i.e., marine) not distant (i.e., terrestrial) sources. The only reasonable explanation is seep bubble plumes –
413 vessel exhaust was ruled out - see **Supp. Material Sect. 2** for more details.

414 FIGURE 5 HERE

415 There was an abrupt drop in CH₄ around 72°N for the outwards transit, which increased again around 75°N.
416 This depressed CH₄ portion of the transit corresponded fairly closely with where the vessel left the warm Murman
417 Coastal Current (**Supp. Fig. S4a**). The strongest anomaly, to 2000 ppb, was observed on the southwards transit
418 where the MCC rises over the sill into the Santa Anna Trough (78.7°N), close to the focus area shown in **Fig. 3**.

419 The two transits were separated by about a month with the September transit higher by ~30 ppb than in August,
420 consistent with strong seasonal CH₄ trends. There were other significant differences. Whereas there were many
421 narrow, implying local, CH₄ anomalies during the southwards transit, there were far more than during the
422 northwards transit and the peak at 78.7°N was not repeated, indicating variability in the emissions.



423 The difference between these transits highlights the challenges of interpreting such snapshot data, supported by
424 the comparison with IASI pixels that were proximal and within several days (**Supp. Fig. S4**). Agreement for the
425 northwards transit was reasonably good (generally within 10 ppb), and generally poor for the southwards transit.

426 **3.2. Focused Study Area Annual Trends**

427 Trends in aggregated pixel “focus areas” are compared for three Barents Sea regions, “Northwest of Barents”
428 including the Greenland Sea and Fram Strait, west of Svalbard (A4-A6), “Northern Barents” in the marginal ice
429 zone at the edge of the Arctic Ocean (A1-A3) and “Southern Barents,” which is strongly under the heat influence of
430 the east fork of the NAC (A7-A10). Of these, A7, A8, and A9 also cover banks – offshore areas of elevated seabed
431 topography. Grouping of focus areas with similar trend patterns into these three Barents Sea regions was based both
432 on physical oceanography and the detailed character of these trends, described below.

433 FIGURE 6 HERE

434 Focus areas with the strongest decreasing ice cover trends are in the marginal ice zone of the northern Barents
435 Sea (south and east of Franz Josef Land), at the southern margin of the Arctic Ocean (**Fig. 6a, A1-A3**). Trends for
436 these three study areas are very similar (after classifying 2006 and 2014 for focus area A3 (Svalbard Northwest) as
437 outliers. Note, focus areas A1-A3 show below-trend ice-free months in 2014 despite no significant 2014 SST
438 deviation, supporting its classification as an outlier (**Fig. 7a**).

439 The similarity in ice coverage trends for area A3 (along the cold Percey Current) with areas A1 and A2 (along
440 the Murman Current’s warm, northward leg) suggests not only increasing northward heat transfer, but also
441 weakening southward cold-water advection. Area A4 (northwest of Svalbard) also shows decreasing ice coverage
442 towards more frequent year-round ice-free status and lies at the Arctic Ocean boundary (**Fig. 6b**), albeit more under
443 the influence of warmer NAC waters than those under the influence of the Murman Current in the north-central
444 Barents Sea (A1-A3). The Central Bank of the Barents Sea (**Fig. 6c, A10**) last saw an ice-covered month in 2005,
445 while a noisy trend of decreasing ice coverage is evident offshore coastal southwest Novaya Zemlya (**Fig. 6c, B9**),
446 along the western fork of the Murman Coastal Current.

447 Overall, all focus areas are trending towards year-round ice-free, with the entire Barents Sea likely to be year
448 round ice free by ~2030 based on an extrapolation of trends in Northern Barents Sea focus areas, A1-A3.

449 FIGURE 7 HERE

450 SST increases in all focus areas (**Fig. 7**) albeit at rates spanning a wide range, from 0.0018 to 0.15 °C yr⁻¹ (see
451 **Table 1**). In the Northern Barents Sea, the strongest warming trend is for area A1, east of Franz Josef Land. This is
452 located in a marginal ice zone, in the path of the warm MC. Area A3 shows the weakest warming trend lies along
453 the cold Percey Current. These trends also are consistent with a strengthening of warm currents and weakening of
454 cold currents inferred from the changes in ice coverage. For the Northwest of Barents focus areas (**Fig. 7b, A4-A6**),
455 the strongest warming is at the northernmost focus area, A4, whereas the weakest trend is for the southernmost focus
456 area (**Fig. 7, A6**). This also is consistent with a strengthened northwards penetration of the warm NAC forming the
457 Bear Island Channel Current (BICC).



458 The strongest warming trend occurs southwest of Novaya Zemlya (**Fig. 7c, A9**) along the path of the northerly
459 turn of the MCC, in shallow water. This trend is consistent with increased eastward MCC penetration east along the
460 coast of Novaya Zemlya and into the Kara Sea. A very weak and highly variable *SST* warming trend is observed to
461 the south of the Svalbard Bank at the intersection of the cold Percey Current and the warm BIC (A7). Areas A10 and
462 A8, and to a lesser extent A9 all show a strong oscillation of ~8 years with peak values in 2005 – 2007, and a
463 minimum around 2010. The same pattern also is observed to the east of Franz Josef Land (areas A1 and A2). All the
464 boxes that exhibit this oscillation lie along the Murman Current, whose origin is in the NAC.

465 FIGURE 8 HERE

466 A positive CH₄ trend is observed across the Barents and Kara Seas from June through September with some
467 regions exhibiting far stronger trends than average (**Supp. Fig. S5**). Areas of faster CH₄ increase include near Franz
468 Josef Land (**Fig. 8a, A1, A2**), the shallower waters offshore W. Svalbard (**Fig. 8b, A4**), and offshore Novaya
469 Zemlya (**Fig. 8c, A9**). These areas of increasing CH₄ correspond to areas of consistent warming for 2003-2015 (**Fig.**
470 **7a, A1, A2**) and consistent warming since ~2004/2005 for southwest offshore Novaya Zemlya and the Central Bank
471 of the Barents Sea (**Fig. 7c, A8-A10**). All these focus areas lie along the northwards flow of the Murman Current
472 and the Murman Coastal Current. In contrast, focus areas along the Percey Current show a slowly decreasing CH₄
473 relative to the trend for the entire Barents Sea (**Fig. 8, A3, A7**), despite an (albeit weakly) increasing *SST*.

474 The strongest CH₄ growth is south of Franz Josef Land (**Table 1 A2**, 3.49 ppb yr⁻¹), followed by offshore
475 northwest Svalbard (**Table 1 A4**, 3.37 ppb yr⁻¹- 2003-2015, 3.6 ppb yr⁻¹ 2005-2015). This positive trend is sustained
476 over the analysis period. This area off the Fram Strait has natural CH₄ seepage associated with hydrate
477 destabilization (Westbrook et al., 2008). This increase is annualized, and thus does not result from shifts in the
478 timing of seasonal warming. Note, the CH₄ slopes for areas A4-A10 all are larger when calculated from the 2005
479 minimum, but not for A1-A3 (**Table 1**). The former lie along the NAC and its eastern current fork, the Murman
480 Current. Neither the Percey Current focus areas (A3, A7) nor other northern Barents Sea focus areas (A1, A2) show
481 this effect depending on the reference time.

482 TABLE 1 HERE

483 The largest variability in *SST* and CH₄ was in the focus area to the north of Murman in the MC (**Table 1, A8**;
484 **Fig. 8**) and likely arises from variations in the strength and location of the MC, which bifurcates around this focus
485 area. Importantly, this area is located above a small, unnamed bank to the south of the Central Bank (**Fig. 2b**).

486 FIGURE 9 HERE

487 3.3. Barents and Kara Sea Climatology

488 Atlantic heat input is very important to the energy budget of the Arctic Ocean and Barents Sea and is driven by
489 the two forks of the NAC (**Fig. 4a**) (Lien et al., 2013). This importance is evident in the Barents Sea *SST*
490 climatology (**Fig. 9**). Warmer water flows eastward along the northern Norwegian and Murman coasts and along the
491 eastern coastline of Svalbard (BIC), and north along the western Svalbard coast. Water becomes cooler as it
492 penetrates eastward, and as it reaches the ice edge. Across much of the Barents Sea there is a strong latitudinal *SST*
493 gradient extending south from the ice edge, independent of the location of the eastern NAC branches. In the coastal



494 waters of Novaya Zemlya, warmer water extends further north than elsewhere. The warm signature disappears in the
495 area where the NAC submerges, near the northern shores of Novaya Zemlya (**Fig. 4a**).

496 FIGURE 10 HERE

497 In June, the warm water extent corresponds fairly well with the median ice edge location, which trends along
498 the location of the cold Percey Current. Southeast of Svalbard, the Percy Current penetrates southward as a narrow
499 extension of cold water ending south of Bear Island. Slightly cooler water is observed over the two banks in the
500 central Barents Sea.

501 The shift to summer *SST* patterns occurs in July, increasing in August, and then beginning to decrease in
502 September (**Supp. Fig. S5**). For north Spitsbergen in the Svalbard archipelago (**Supp. Fig. S1**) the northerly cold
503 Spitsbergen Coastal Current (SCC) inshore of the West Spitsbergen current (WSC) breaks down. This suggests the
504 SCC is entrained by the more energetic WSC (McClimans, 1994), flowing northwards along southwest Spitsbergen
505 underneath colder surface waters, likely below strong summer stratification. The WSC warm water is further
506 offshore the west coast of Svalbard in June than in September (**Supp. Fig. S1**), i.e., the Barents Front shifts
507 shoreward in summer.

508 By September, *SST* in the shallower eastern (coastal) Barents Sea has warmed to levels comparable to the
509 warmer waters in the southwest Barents Sea where NAC heat input maintains elevated *SST*. Warmer *SST* also
510 extends further offshore Norway and Murman. These seasonal *SST* changes match the sea ice's northwards retreat to
511 Franz Josef Land (**Fig. 10b**). However, Barents Sea warming does not follow the ice edge between Svalbard and
512 Franz Josef Land, corresponding instead to the location of the Percy Current. Still, whereas warm water is more
513 extensive in south and east Barents Sea in September than August, in the northwest, cold water associated with the
514 Percy Current has expanded from August to September (**Supp. Fig. S5**).

515 The now mostly ice-free Kara Sea in September exhibits coastal warming, particularly to the east, where there
516 also is heat input from the Ob and Yenisei Rivers (east of the Yamal Peninsula). This area exhibits evident warming
517 despite partial ice coverage of the Gulf of Ob in June and likely is driven by warmer riverine water inputs.

518 CH_4 concentrations show a clear latitudinal trend that increases towards the north. This latitudinal gradient is
519 weak in June and strong in September. Strong localized variations also occur in different Barents Sea regions. CH_4
520 concentrations along the Murman Current and in the (ice-covered) Kara Sea largely are below the latitudinal mean
521 in June, whereas west of Svalbard and in the north-central Barents Sea they are above average.

522 In June, CH_4 is depressed strongly around Svalbard and around Franz Josef Land and Novaya Zemlya. For
523 Svalbard, this corresponds to the SCC that hugs the shore. By September, CH_4 concentrations are notably different
524 with significantly higher CH_4 and a distinctly different spatial distribution. Most notable is the shift from depressed
525 to strongly enhanced CH_4 in the region to the west of Novaya Zemlya and around the Franz Josef Land archipelago.
526 Strong CH_4 enhancement also occurs in the outflow plumes of the Ob and Yenisei Rivers in the Kara Sea, around
527 the Taymyr Peninsula. Around Svalbard, CH_4 has risen to near latitudinal mean levels in September, except for
528 offshore north Spitsbergen and Nordaustlandet, where sea ice remains.



529 3.3. Barents and Kara Seas Trends

530 Across the Barents Sea, a number of different focus areas with distinct *SST* and CH_4 trends are identified (**Fig.**
531 **7**). These manifest significant spatial heterogeneity at the pixel scale and at the focus-area size scale. We analyze
532 trends in aggregated-pixel “focus areas” located in key regions where *SST* change is the strongest (**Sec. 3.3**; **Supp.**
533 **Fig. S6** for July and August trends).

534 June *SST* warming trends are fairly different from September *SST* trends (**Fig. 11**). In June, warming occurs
535 much faster in the eastern Barents Sea, specifically, in waters affected by the Murman Coastal Current (MCC). This
536 suggests the magnitude of atmospheric cooling during transit from the Atlantic is decreasing. Warming occurs
537 primarily in shallow (generally less than 100-m deep) (**Fig. 11b**) waters that are generally well mixed. Sea ice is
538 gone in this region by March-May, later in more northerly areas (**Fig. 4b**). Whereas there is no clear warming trend
539 in July and August; a strong warming trend appears in the Kara Sea by September (**Supp. Fig. S5**). This warming
540 trend occurs several months after the ice retreat – Kara Sea is ice-free in July (**Supp. Fig. S5**). This suggests
541 increasing MCC penetration into the Kara Sea. Loeng (1991) reported that MCC penetration into the Kara Sea was
542 uncommon in the middle of the 20th century.

543 **FIGURE 11**

544 More rapid warming occurs offshore of the western coast of Novaya Zemlya from June-September. This is
545 where the Murman Current (MC) transports water towards the St Anna Trough (the dominant Barents Sea outflow),
546 a region where shoaling is likely based on seabed topography (**Fig. 2b**) (Maslowski et al., 2004). The MC then flows
547 (and submerges under ice and Arctic surface water) along the east shores of Franz Josef Land. Accelerated warming
548 diminishes near the northern margin of the Kara Sea, where river outflow dominates the oceanography.

549 Enhanced warming also occurs to the south and to the west-northwest of Svalbard in September, following
550 approximately the trend of the northerly fork of the NAC. In contrast, waters off east Svalbard, where the East
551 Spitsbergen Current (ESC) transports cold Arctic waters southwards, do not exhibit a significant warming trend in
552 September, although it does exhibit a warming trend in July. This suggests changes in the seasonal trends of PC's
553 penetration into the Barents Sea, likely modulated by seasonal ice sheet retreat. There is no significant warming in
554 either June or September in waters to the north of Franz Josef Land with ice-coverage persisting through September.

555 Overall Barents Sea atmospheric CH_4 is increasing (**Fig. 10C**), consistent with the global CH_4 trend (Nisbet et
556 al., 2014). However it is notable that some Arctic regions exhibit significantly more rapidly increasing CH_4 than the
557 global or Barents Sea trends. In June, CH_4 trends are largely similar in both ice-free and ice-covered areas. In near-
558 coastal waters around Svalbard (except the east), in northern Norwegian fjords, and for the White Sea (Murmansk)
559 where CH_4 growth trends are elevated.

560 CH_4 trends in September, when ice coverage has retreated to the northern edge of the Barents and Kara Seas
561 (**Fig. 10b**), are very strongly enhanced in the East Barents Sea and the South Kara Sea. These areas coincided with
562 areas of enhanced *SST* warming and show CH_4 trends almost three times as high as the general Arctic trend. In
563 contrast, regions without enhanced warming, particularly waters affected by cold currents, exhibit the weakest CH_4
564 growth trend though slightly above the overall Barents Sea trend. In the Kara Strait between the Barents and Kara
565 Seas, CH_4 increases very strongly.



566 Enhanced CH₄ growth is not evident in either June or September to the north of Svalbard, despite strong SST
567 increases; however, significant increases are evident here in August. This follows significant CH₄ enhancement in
568 July to the southeast of Svalbard. This July-August shift follows the NAC.

569 4. Discussion

570 4.1. Methane transport from the seabed to the atmosphere

571 In this study, we hypothesized that lower tropospheric CH₄ correlates both with changes in the overall water
572 column temperature and with SST changes, both satellite remote sensing products. For this analysis, we also
573 considered the locations of currents and trends in these currents, seabed bathymetry, prevailing winds, and available
574 Barents Sea, water-column temperature data – primarily the long-term Kola Section data, which due to the
575 importance of the Murman Current was directly relevant.

576 The proposed source of the atmospheric CH₄ anomaly is seabed seepage from either thermogenic sources, i.e.,
577 petroleum hydrocarbon reservoirs (Judd and Hovland, 2007), or degradation of submerged permafrost and hydrates
578 (Shakhova et al., 2017). Both permafrost and hydrate deposits can include both thermogenic and biogenic CH₄.

579 These emissions largely are as bubbles (Judd and Hovland, 2007) because the microbial filter generally removes
580 aqueous-enriched CH₄ fluid emissions from sediments to the water column (Reeburgh, 2003). As a bubble rises, it
581 loses CH₄ to the water column by dissolution, transporting the remainder. Larger bubbles vertically transport a
582 greater fraction of their contents more efficiently than smaller bubbles (Leifer and Patro, 2002). Some portion of the
583 dissolved fraction is transported vertically by the bubble-driven upwelling flow (Leifer et al., 2009). The remaining
584 fraction may either diffuse to the atmosphere by turbulence or be oxidized microbially. In the deep sea, all the
585 dissolved CH₄ likely is oxidized, where given the relevant depth scale is the winter wave mixed layer (WWML)
586 based on microbial oxidation timescales (Rehder et al., 1999). The Arctic WWML can extend to 100-200 m. In
587 shallow water (e.g., less than 20 m), most seep bubble CH₄ reaches the sea surface, with the portion decreasing for
588 smaller bubbles or depth (Leifer and Patro, 2002). For example, Leifer et al. (2017) showed that for the Laptev Sea
589 that ~25% of seabed CH₄ from 70 m reaches the sea surface directly, consistent with sonar observations of bubble
590 plumes reaching the sea surface (Leifer et al., 2017). CH₄ that is deposited deeper in the wave mixed layer (WML)
591 likely diffuses to the atmosphere rapidly, although stratification powerfully suppresses this transport. Storms
592 breakdown this stratification (Leifer et al., 2015) sparging all the dissolved CH₄ to the atmosphere (Shakhova et al.,
593 2013). Thus, CH₄ emissions that are deposited (by dissolution) into the WWML but below stratification may escape
594 many months later and distant from their seabed origin. In the process, the dissolved CH₄ drifts with currents, which
595 if driven upslope, transports the CH₄ to shallower depths, potentially into the WML where it can escape to the
596 atmosphere, termed shoaling.

597 In practical terms, bubble transport means that seepage extends the depth of the WWML for CH₄ by 50-100 m,
598 i.e., 150-300 m, extending the depth that storms can sparge dissolve CH₄ to the atmosphere. This implies, CH₄ from
599 seabed seepage over a significant fraction of the Barents Sea (**Fig. 2b**) can reach the WWML, or can be transported
600 by currents into shallower waters (shoaling) into the WWML.



601 The above discussion was for non-oily seepage. However, where seepage arises from a petroleum hydrocarbon
602 reservoir, bubbles likely are oily. Oil slows bubble rise (Leifer, 2010) but reduces dissolution dramatically, allowing
603 their survival to far higher in the water column than non-oily bubbles (Leifer and MacDonald, 2003). Oily bubbles
604 can reach the sea surface from the deep sea due also to processes associated with hydrates, for example MacDonald
605 et al. (2010) tracked seabed seep bubbles by ROV from 1 km to the WML (upper 20 m), causing a significant
606 positive CH₄ anomaly in the surface waters. Given the presence of extensive proven and proposed petroleum
607 reservoirs across the Barents and Kara Seas (Rekacewicz, 2005), it is likely that some Barents Sea seepage is oily
608 bubbles, enhancing CH₄ transport to the sea surface.

609 Positive, localized, atmospheric CH₄ anomalies can reflect local seabed production and vertical transport to the
610 atmosphere, or lateral near-seabed transport and shoaling that elevates the dissolved CH₄ into the WML and then air
611 sea exchange into the atmosphere, or transport from a distant source. Detangling these processes leverages the
612 strength of the continuous and synoptic view of satellite datasets compared to the high spatial and temporal
613 resolution snapshot provided by field campaigns.

614 One unlikely source of CH₄ anomalies for the Barents and Kara Seas is atmospheric transport as there is neither
615 significant local industry, nor extensive wetlands/terrestrial permafrost nearby and downwind for the prevailing
616 winds. Note – synoptic systems can transport CH₄ from northern Europe or Russia to the Barents Sea area, but
617 synoptic system winds are not dominant (prevailing) and thus play a small role in a time-averaged dataset.
618 Moreover, these terrestrial sources are distant, implying extensive anomaly size scale in the Barents Sea.
619 Additionally, they would decrease with distance from northern Europe. Instead, the anomalies are localized and
620 decrease towards Europe. Although the oil production and pipeline infrastructure on the Yamal Peninsula and near
621 Kolguyev Island (**Supp. Fig. S7**) likely are strong CH₄ sources, they are downwind of the prevailing winds for the
622 Barents and Kara Seas.

623 **4.2. Local versus Transported and the Importance of Shoaling**

624 In this study we explore the likelihood that atmospheric CH₄ anomalies result from local generation and vertical
625 transport to the sea surface, versus distant lateral transport by currents prior to vertical transport to the sea surface.

626 Areas of accelerated CH₄ increasing trends were closely related to the path of the Murman Current as it flows
627 towards the Kara Strait rather than depth (**Fig. 11**). Both the rising seabed bathymetry and the presence of both
628 southwards and northwards currents through the Kara Strait imply strong mixing and thus transport to the
629 atmosphere. Along this path are significant offshore petroleum hydrocarbon reservoirs, which could be seeping CH₄
630 into the waters of the Murman Current. Further evidence for transport and shoaling is the spatial distribution of CH₄
631 around Kolguyev Island (north of the White Sea), which increases faster on its western side than its eastern side,
632 even though the sea to the island's east is shallower. In fact the CH₄ spatial pattern correlates better with shadowing
633 in the island's lee from shoaling currents, rather than with seabed depth. Prevailing winds are from the south-
634 southeast / north-northeast (Kubryakov et al., 2016), thus atmospheric transport cannot explain the pattern, which
635 would be consistent with easterly winds.



636 In the Kara Sea, the correlation of enhanced CH₄ with depth is poor, which is shallower to the north. Instead,
637 the location of enhanced September CH₄ closely matches the location of oil and gas reserves, e.g., **Supp. Fig. S7**
638 and Rekecewicz (2005) and also along the path of warm water transport by the Murman Coastal Current as it enters
639 the Kara Sea and then follows the coastline of the Kanin Peninsula. Although there are extensive oil and gas
640 production on the Yamal Peninsula, prevailing winds blow away from the Barents Sea. Note, the trend shows an
641 acceleration of CH₄ growth, implying increasing emissions, i.e., not steady-state seabed warming but accelerating
642 seabed warming. This increasing CH₄ growth is for September, not June, corresponding to when the water column is
643 warmest in the South Barents Sea (Stiansen et al., 2009). Also, the Barents Sea outflow through St Anna's Trough is
644 greater (about double) than June (Gammelsrød et al., 2009) when the growth in the CH₄ anomaly occurs (**Fig. 11d**).
645 The importance of this transport also is apparent in the *SST* trend with the greatest warming occurring in June in the
646 southeast Barents Sea (offshore the Kanin Peninsula) near the Kara Strait. This region lies to the west of the areas of
647 accelerating CH₄ growth in September near the Kara Strait. In contrast, significant *SST* warming is not observed in
648 September in this easternmost region of the Barents Sea.

649 Two other areas of accelerating CH₄ growth lie in the north-central Barents Sea, north of Central Bank, and
650 offshore northern Novaya Zemlya. These regions lie along the pathway of the Murman Current, which is an
651 extension of the warm NAC and the largest northwards transport of Barents Sea water (Lien et al., 2013). Water
652 flowing in this direction also is forced upwards – from 300-400 m to just 100 m as it crosses a sill into the St. Anna
653 Trough with rising seabed towards the east and towards Novaya Zemlya with water depths of tens of meters (**Fig.**
654 **2B**). Additionally, this region of accelerating CH₄ growth corresponds spatially to potential (unproven) gas and oil
655 reserves that extend across the St Anna Trough to Franz Josef Land (**Supp. Fig. S7**; (Rekecewicz, 2005)).

656 There are proven oil and gas fields to the south, along the path of the Murman Current, but south of the area of
657 accelerating CH₄. Again, there is good spatial correlation with these proposed reservoirs. Notably, the enhanced CH₄
658 around Franz Josef Land does not correlate with the potential reserves, but does correlate with depth and the flow of
659 the Murman Current, consistent with shoaling. Although some of the accelerating CH₄ near Novaya Zemlya could
660 arise from increasing local seabed emissions, seabed temperatures were below zero until 2009 (Boitsov et al., 2012),
661 which would imply submerged permafrost and/or hydrate deposits here have not yet degraded significantly,
662 supporting both a transport and a shoaling mechanism.

663 **4.3. Sea Surface Temperature**

664 The analysis shows that CH₄ growth from portions of the Barents and Kara Seas is accelerating faster than the
665 Barents Sea mean and the latitudinal mean. To some level these correlate with accelerating *SST* warming, but the
666 correlation is poor. One factor underlying this is the delay between *SST* warming and ocean column warming of
667 several months (Stiansen et al., 2009). There also appears to be a several year response time; the ~6-8 year
668 oscillation in the *SST* trend in the Southern Barents Sea (areas A8, A9, and A10) has a very similar timescale to the
669 seabed trends reported by Boitsov et al. (2012) but precedes it by ~2-4 years.

670 More rapid warming occurs offshore Novaya Zemlya moving northwards from June-September, where the
671 Murman Current transports water and the seabed topography is likely to cause shoaling. This suggests warmer



672 terrestrial weather is not driving Kara Sea changes as this would occur uniformly both in the south Kara Sea, which
673 is influenced by the Barents Sea, and the northern Kara Sea, which is influenced by river outflow. Additionally, if
674 increased riverine heat input was driving the trend, the greatest acceleration would be in the northern Kara Sea,
675 which also is shallower.

676 There are a number of possible explanations for why *SST* is warming fastest in regions along the Murman
677 Current and NAC. One is sea-ice retreat; however, the warming occurs several months after the retreat of the sea ice.
678 Another is that currents are transporting warmer water; however, then warming would occur all along the pathway
679 of the current. Third is that stratification is becoming shallower, allowing more cooling to the atmosphere. This
680 would imply a weakening of storms and winds – which firstly is inconsistent with warmer *SST*, and secondly, there
681 is no indication that Barents Sea storminess is changing or progressing further northwards (Koyama et al., 2017).
682 Another possibility is that currents are strengthening. Stronger currents could relate to larger oceanographic trends.
683 Seabed September temperatures (Boitsov et al., 2012) do not suggest increased warmer seabed temperatures north of
684 Norway and Russia, but do suggest warmer seabed temperatures to the east and also along Novaya Zemlya –
685 suggesting a greater importance of the MC. This is consistent with the model of McClimans et al. (2000) that
686 currents are pushing the marginal ice zone. The warming trend suggests a strengthening of the seasonal trend in the
687 Barents Sea outflow, which is greater in September than June (Gammelsrød et al., 2009).

688 The strongest warming trend is for the shallow water off northwest Svalbard (area A4) (**Fig. 11b**), which also
689 exhibited the strongest acceleration of CH₄ growth for around Svalbard. In this area, seabed topography is nearly
690 level over an extensive shelf with depths in the range 250-400 m. Where the shelf falls off sharply, rising sea
691 temperatures will minimally induce hydrate destabilization. In contrast, where the shelf falls off very gently, small
692 temperature increases shift extensive areas of seabed from below to above the hydrate stability field. This area is
693 immediately to the north of the area where several researchers have identified extensive seabed seep CH₄ emissions
694 (Mau et al., 2017; Myhre et al., 2016; Westbrook et al., 2009). The most likely explanation is a strengthening of the
695 West Spitsbergen Current, discussed below, and shifts in the Barents Sea Front.

696 **4.4. Implications for Svalbard Area Emissions**

697 There are few atmospheric and ocean CH₄ data for the Barents Sea and surrounding areas, the most prominent
698 being associated with CH₄ seepage off Spitsbergen, Svalbard, located immediately south of focus area A4. Studies
699 to date have been in early summer; Mau et al. (2017); Myhre et al. (2016) who made measurements in the
700 atmosphere and water column; Westbrook et al. (2009) reported sonar observations of seep bubbles for August-
701 September, and slightly elevated aqueous CH₄ in surface waters immediately above the bubble plumes. All
702 concluded transport to the atmosphere was not significant, attributed to trapping of dissolved CH₄ below a sharp
703 pycnocline. It is important to note that with respect to the overall Barents Sea area CH₄ anomaly, the Svalbard area
704 is far less important than around Franz Josef Land, off the west coast of Novaya Zemlya, and the north-central
705 Barents Sea (**Fig. 10**).

706 Both *SST* and CH₄ in June (**Fig. 10**) and July (**Supp. Fig. S5**) for west Svalbard show that much of the area of
707 active seepage was inshore of the Barents Sea Front, and thus under the cooling Arctic waters of the Spitsbergen



708 Coastal Current (SCC), supported by reported salinity data (Mau et al., 2017). Although the *SST* remains suppressed
709 off Spitsbergen in September, and extends further offshore, CH₄ concentrations no longer are depressed compared to
710 Atlantic water further offshore, i.e., greater transport to the atmosphere. Such transport would not be expected
711 downcurrent (north) of the bubble plumes observed by the early fall cruise reported in Westbrook et al. (2009).

712 Although data indicate these seeps do not contribute to summer atmospheric CH₄, this study suggests that the
713 emitted CH₄ likely is reaching the atmosphere far downstream where currents shoal. Interestingly, Mau et al. (2017;
714 Fig. 3) show data that could be interpreted as shoaling with elevated aqueous CH₄ forced shallower by the north-
715 flowing SCC, rising as it crosses onshore-offshore aligned subterranean ridges. Focus area A4 shows strong increase
716 in CH₄ from 2005-2015 (the strongest of the focus areas (**Table 1**) and in increasing *SST* over this time period,
717 consistent with shoaling. Larger acceleration of CH₄ growth is observed north of Spitsbergen in June (**Fig. 11c**),
718 which is the most likely location for shoaling based on detailed Svalbard bathymetry and currents (**Supp. Fig. S2**).
719 Specifically, this is where some of the warm West Spitsbergen Current mixes with the cold, Spitsbergen Coastal
720 Current (SCC) that would be CH₄ enriched from seabed seepage, and then flows over relatively shallow seabed
721 towards the Hinlopen Strait. To summarize, although there is evidence of increasing downcurrent CH₄ transport to
722 the atmosphere downcurrent of seepage off West Svalbard after shoaling, it is not significant with respect to overall
723 Barents Sea emissions.

724 There is evidence of acceleration in the CH₄ growth nearshore off western Svalbard in June, but not in
725 September (**Fig. 11**) when CH₄ growth acceleration lies in the further offshore waters that are impacted by the warm
726 WSC. Trends in *SST* also suggest a weakening of the Percey Current in June and more so in September. Given that
727 from June to September the SCC extends further offshore, this suggests WSC control. Similarly, the WSC eastwards
728 leg that crosses Nordaustlandet is driving a rapid increase in *SST* in September and likely relates to the increased
729 CH₄ trend.

730 **4.5. Ice-Free Barents Sea**

731 The ice coverage trend shows that northeast Barents and southern Barents Sea already are ice-free or near ice-
732 free year round, whereas northwest Barents Sea (around Franz Josef Land and St. Anna Trough) remains ice-
733 covered for about half the year. The ice coverage trends (**Fig. 6**) suggest most of the Barents Sea will be ice free,
734 year-round in another decade and a half, circa 2030. This is comparable to the 2023-2036 estimate of Onarheim and
735 Årthun (2017; Fig. 3), which also notes that the current decreasing trend lies outside the oscillation envelope since
736 1850.

737 This has implications for the Barents and Kara Seas ecosystems, and follows changes that have been
738 documented across the Arctic in satellite remote sensing of phytoplankton concentration (Arrigo et al., 2008; Arrigo
739 and van Dijken, 2011; Kahru et al., 2011) and *in situ* studies (Grebmeier et al., 2015; Grebmeier et al., 2006). One
740 example is a significant northwards shift (5° over 20 yrs.) of phytoplankton blooms (Neukermans et al., 2018). Ice
741 cover changes play a key role. For example, primary productivity increases in the northern Barents and Kara Seas
742 (**Fig. 2**) are considered caused by decreased ice cover (Slagstad et al., 2015), which has driven changes in the higher
743 trophic levels of the pelagic and benthic community (Grebmeier et al., 2015).



744 The Barents Sea is a marginal sea between the temperate Norwegian Sea and the Arctic Ocean and thus is the
745 conduit through which lower-latitude oceanic heat is transmitted to the Arctic Ocean (Onarheim and Årthun, 2017).
746 Given the significant role the Barents Sea plays in overall Arctic ice loss - fully 25% of the loss is attributed to the
747 Barents Sea, which comprises 4% of the Arctic Ocean and marginal seas (Smetsrud et al., 2013), implications will
748 be significant for weather including at lower latitudes, and the marine ecosystem. Seemingly counter-intuitively, the
749 reduction of sea ice increases the upwards surface heat flux as ice has an insulating effect. Thus ice-loss somewhat
750 stabilizes Arctic Ocean ice, particularly during winter (Onarheim and Årthun, 2017) and may even lead to growth of
751 ice in the Arctic and Northern Greenland Seas. Still, the data herein showed a progressive weakening of the Percey
752 Current, which will continue to cause ice loss off east Svalbard and warming of these waters. This agrees with
753 Alexander et al. (2004) who concluded that the (semi-stationary due to bathymetry) Polar Front has shifted to
754 domination of Atlantic water over Arctic waters.

755 As already seen, though, the progression of ice loss in the south and east Barents Sea along the pathway of the
756 Murman Coastal Current has led to a progressive loss of ice in the south Kara Sea. Thus, the balance between the
757 two processes – heat loss to the atmosphere from and progressive transport of heat by currents to the Kara Sea are
758 clearly shifting towards warmer. The implications of decreasing ice coverage in the shallow Kara Sea are significant
759 with respect to CH₄ emissions – the area is rich in hydrocarbon resources that currently are sequestered (albeit data
760 show already poorly) under submerged permafrost that will continue to degrade, while warming seabed
761 temperatures will enhance microbial degradation of the vast organic material deposited over the millennia by the Ob
762 and Yenisei Rivers. Thus, the already significant importance of Arctic CH₄ anomaly from the Kara Sea will
763 accelerate due to feedbacks from an ice-free Barents Sea.

764 4.6. Future research

765 Long-term oscillations with a timescale of 6-8 years were identified (e.g., **Fig. 9**); however, the length of the
766 dataset (13 years) is too short to investigate this in detail. Extending the analysis to include more recent data (say
767 through 2020) would span a full 2 1/2 cycles and allow investigation of correlations with other driving
768 oceanographic atmospheric cycles, such as the NAO. This would be particularly valuable given that recent data
769 show that the most recent two years are the most extreme in terms of Barents Sea ice coverage Oziel et al. (2016)
770 and CH₄ anomaly (**Supp. Fig. S8; Supp. Video**). Extending the analysis forward in time clearly would provide
771 greater insights into the complex relationship between currents and CH₄ emissions. In this regard, the long CH₄ time
772 series planned to be collected by the IASI satellite series through the 2030s (Onarheim and Årthun, 2017) will be
773 invaluable.

774 Additionally, there is clearly need for these data to be incorporated into coupled atmospheric-oceanographic-ice
775 models to understand in greater detail the processes underlying the changes, improving the ability to forecast trends
776 in Arctic marine greenhouse gas emissions. Currently the strong and growing CH₄ anomaly from Novaya Zemlya
777 and Franz Josef Land are the strongest in the Arctic, yet are not yet incorporated (or identified) in inversion models,
778 e.g., Crevoisier et al. (2014). This identifies a key strength of satellite data, which can identify sources that are not
779 part of an a priori.



780 Finally, as part of this study, changes in chlorophyll were investigated with respect to changes in *SST* and CH_4 .
781 These relationships need to be evaluated in future research to tie the dramatic changes in the Barents and Kara Sea
782 ecosystem to physical changes in oceanography, leveraging the strengths of satellite data.

783 5. Conclusion

784 In this study, the synoptic, repeat nature of satellite data was used to investigate the relationship between
785 currents, and trends in sea surface temperature, ice extent, and methane (CH_4) anomaly for the Barents and Kara
786 Seas for 2003-2015. Large positive CH_4 anomalies were discovered around Franz Josef Land archipelago and
787 offshore west Novaya Zemlya in September, in areas where currents shoal, with far smaller CH_4 enhancement
788 around Svalbard, again, strongest where currents likely shoal, downcurrent of seabed seepage. This highlights a
789 major strength of satellite data: Identification of sources that are not part of an a priori in inversion models.

790 The strongest *SST* increase was southeast Barents Sea in June due to strengthening of the warm Murman
791 Currents (an extension of the Norwegian Atlantic Current) and in the south Kara Sea in September, whereas the cold
792 Percey Current weakened. These two regions also exhibit the strongest CH_4 growth acceleration as well as around
793 Franz Josef Land. Likely sources are CH_4 seepage from extensive oil and gas reservoirs underlying the central and
794 east Barents Sea and Kara Sea; however, the spatial pattern was poorly correlated with depth and best correlated
795 with strengthening current that shoal.

796 If current trends continue, then heat flows to the Barents Sea and Kara Sea by strengthening currents will lead to
797 an ice free Barents Sea free in about 15 years, while driving seabed warming and enhanced CH_4 emissions,
798 particularly from areas where currents drive shoaling.

799

800 **Acknowledgements:** The research was supported by a grant from NASA ROSES2013: “A.28, THE SCIENCE OF
801 TERRA AND AQUA: Long-term Satellite Data Fusion Observations of Arctic Ice Cover and Methane as a Climate
802 Change Feedback.” We thanks Vladimir Ivanov, Arctic and Antarctic Research Institute, for organizing the NABOS
803 cruise and Cathrine Lund Myrhe, Norwegian Air Research Institute (NILU), for calibration gas used during the
804 NABOS cruise.

805 **References**

- 806 Aagaard, K. and Carmack, E. C.: The role of sea ice and other fresh water in the Arctic circulation,
807 *Journal of Geophysical Research: Oceans*, 94, 14485-14498, 1989. doi: 10.1029/JC094iC10p14485
- 808 Ackerman, S., Strabala, K., Menzel, P., Frey, R. A., Moeller, C., and Gumley, L. E.: Discriminating clear-
809 sky from cloud with {MODIS}, Algorithm Theoretical Basis Document (MOD35), ATB-MOD-06,
810 129 pp., 2010. http://modis.gsfc.nasa.gov/data/atbd/atbd_mod06.pdf
- 811 Ackerman, S. A., Strabala, K. I., Menzel, W. P., Frey, R. A., Moeller, C. C., and Gumley, L. E.:
812 Discriminating clear sky from clouds with MODIS, *Journal of Geophysical Research: Atmospheres*,
813 103, 32141-32157, 1998. doi: 10.1029/1998jd200032
- 814 AIRS: <http://airs.jpl.nasa.gov/data/v6/>, <http://airs.jpl.nasa.gov/data/v6/>, 2016.
- 815 AIRS Science Team/Joao Teixeira: AIRS2RET: AIRS/Aqua L2 Standard Physical Retrieval (AIRS-only)
816 V006. Goddard Earth Sciences Data and Information Services Center (GES DISC), Greenbelt, MD,
817 2016.
- 818 Alexander, M. A., Bhatt, U. S., Walsh, J. E., Timlin, M. S., Miller, J. S., and Scott, J. D.: The atmospheric
819 response to realistic Arctic sea ice anomalies in an AGCM during winter, *Journal of Climate*, 17, 890-
820 905, 2004. doi: 10.1175/1520-0442(2004)017<0890:Tartra>2.0.Co;2
- 821 Alexander, M. A., Scott, J. D., Friedland, K. D., Mills, K. E., Nye, J. A., Pershing, A. J., and Thomas, A.
822 C.: Projected sea surface temperatures over the 21st century: Changes in the mean, variability and
823 extremes for large marine ecosystem regions of Northern Oceans, *Elementa Science of the*
824 *Anthropocene*, 6, 9, 2018. doi: 10.1525/elementa.191
- 825 Aliabadi, A. A., Staebler, R. M., de Grandpré, J., Zadra, A., and Vaillancourt, P. A.: Comparison of
826 estimated atmospheric boundary layer mixing height in the Arctic and Southern Great Plains under
827 statically stable conditions: Experimental and numerical aspects, *Atmosphere-Ocean*, 54, 60-74,
828 2016. doi: 10.1080/07055900.2015.1119100
- 829 Archer, D., Buffett, B., and Brovkin, V.: Ocean methane hydrates as a slow tipping point in the global
830 carbon cycle, *Proceedings of the National Academy of Sciences*, 106, 20596-20601, 2009. doi:
831 10.1073/pnas.0800885105
- 832 Arrigo, K. R., van Dijken, G., and Pabi, S.: Impact of a shrinking Arctic ice cover on marine primary
833 production, *Geophysical Research Letters*, 35, L19603, 2008. doi: 10.1029/2008GL035028
- 834 Arrigo, K. R. and van Dijken, G. L.: Secular trends in Arctic Ocean net primary production, *Journal of*
835 *Geophysical Research: Oceans*, 116, C09011, 2011. doi: 10.1029/2011JC007151
- 836 Aumann, H. H., Chahine M.T., Gautier, C., Goldberg, M. D., Kalnay, E., McMillin, L. M., Revercomb,
837 H., Rosenkranz, P. W., Smith, W. L., Staelin, D. H., Strow, L. L., and Susskind, J.:
838 AIRS/AMSU/HSB on the Aqua mission: design, science objectives, data products, and processing
839 systems, *IEEE Transactions on Geoscience and Remote Sensing*, 41, 253-264, 2003a. doi:
840 10.1109/TGRS.2002.808356
- 841 Aumann, H. H., Chahine, M. T., Gautier, C., Goldberg, M. D., Kalnay, E., McMillin, L. M., Revercomb,
842 H., Rosenkranz, P. W., Smith, W. L., Staelin, D. H., Strow, L. L., and Susskind, J.:
843 AIRS/AMSU/HSB on the Aqua mission: design, science objectives, data products, and processing
844 systems, *IEEE Transactions on Geoscience and Remote Sensing*, 41, 253-264, 2003b. doi:
845 10.1109/TGRS.2002.808356
- 846 Biraud, S. C.: ARM-ACME V: ARM Airborne Carbon Measurements V on the North Slope of Alaska
847 Field Campaign Report, DOE Office of Science Atmospheric Radiation Measurement (ARM)
848 Program (United States), 15 pp., 2016.
- 849 Boitsov, V. D., Karsakov, A. L., and Trofimov, A. G.: Atlantic water temperature and climate in the
850 Barents Sea, 2000–2009, *ICES Journal of Marine Science*, 69, 833-840, 2012. doi:
851 10.1093/icesjms/fss075
- 852 Bovensmann, H., Burrows, J. P., Buchwitz, M., Frerick, J., Noël, S., Rozanov, V. V., Chance, K. V., and
853 Goede, A. P. H.: SCIAMACHY: Mission objectives and measurement modes, *Journal of the*



- 854 Atmospheric Sciences, 56, 127-150, 1999. doi: 10.1175/1520-
855 0469(1999)056<0127:smoamm>2.0.co;2
- 856 Carmack, E. and McLaughlin, F.: Towards recognition of physical and geochemical change in Subarctic
857 and Arctic Seas, *Progress in Oceanography*, 90, 90-104, 2011. doi: 10.1016/j.pocean.2011.02.007
- 858 Chang, R. Y.-W., Miller, C. E., Dinardo, S. J., Karion, A., Sweeney, C., Daube, B. C., Henderson, J. M.,
859 Mountain, M. E., Eluszkiewicz, J., Miller, J. B., Bruhwiler, L. M. P., and Wofsy, S. C.: Methane
860 emissions from Alaska in 2012 from CARVE airborne observations, *Proceedings of the National
861 Academy of Sciences*, 111, 16694-16699, 2014. doi: 10.1073/pnas.1412953111
- 862 Clark, R. N., Curchin, J. M., Hoefen, T. M., and Swayze, G. A.: Reflectance spectroscopy of organic
863 compounds: 1. Alkanes, *Journal of Geophysical Research*, 114, E03001, 2009. doi:
864 10.1029/2008je003150
- 865 Clerbaux, C., Boynard, A., Clarisse, L., George, M., Hadji-Lazaro, J., Herbin, H., Hurtmans, D.,
866 Pommier, M., Razavi, A., Turquety, S., Wespes, C., and Coheur, P.-F.: Monitoring of atmospheric
867 composition using the thermal infrared IASI/MetOp sounder, *Atmospheric Chemistry and Physics*, 9,
868 6041-6054, 2009. doi: 10.5194/acp-9-6041-2009
- 869 Cohen, J., Screen, J. A., Furtado, J. C., Barlow, M., Whittleston, D., Coumou, D., Francis, J., Dethloff,
870 K., Entekhabi, D., Overland, J., and Jones, J.: Recent Arctic amplification and extreme mid-latitude
871 weather, *Nature Geoscience*, 7, 627, 2014. doi: 10.1038/ngeo2234
- 872 <https://www.nature.com/articles/ngeo2234-supplementary-information>
- 873 Comiso, J. C.: Large decadal decline of the arctic multiyear ice cover, *Journal of Climate*, 25, 1176-1193,
874 2012. doi: 10.1175/jcli-d-11-00113.1
- 875 Comiso, J. C., Parkinson, C. L., Gersten, R., and Stock, L.: Accelerated decline in the Arctic sea ice
876 cover, *Geophysical Research Letters*, 35, L01703, 2008. doi: 10.1029/2007GL031972
- 877 Crevoisier, C., Clerbaux, C., Guidard, V., Phulpin, T., Armante, R., Barret, B., Camy-Peyret, C.,
878 Chaboureaud, J. P., Coheur, P. F., Crépeau, L., Dufour, G., Labonnote, L., Lavanant, L., Hadji-Lazaro,
879 J., Herbin, H., Jacquinet-Husson, N., Payan, S., Péquignot, E., Pierangelo, C., Sellitto, P., and
880 Stubenrauch, C.: Towards IASI-New Generation (IASI-NG): Impact of improved spectral resolution
881 and radiometric noise on the retrieval of thermodynamic, chemistry and climate variables,
882 *Atmospheric Measurement Techniques*, 7, 4367-4385, 2014. doi: 10.5194/amt-7-4367-2014
- 883 Desjardins, R. L., Worth, D. E., Pattey, E., VanderZaag, A., Srinivasan, R., Mauder, M., Worthy, D.,
884 Sweeney, C., and Metzger, S.: The challenge of reconciling bottom-up agricultural methane
885 emissions inventories with top-down measurements, *Agricultural and Forest Meteorology*, 248, 48-
886 59, 2018. doi: <https://doi.org/10.1016/j.agrformet.2017.09.003>
- 887 Dickson, R. R., Osborn, T. J., Hurrell, J. W., Meincke, J., Blindheim, J., Adlandsvik, B., Vinje, T.,
888 Alekseev, G., and Maslowski, W.: The Arctic Ocean response to the North Atlantic Oscillation,
889 *Journal of Climate*, 13, 2671-2696, 2000. doi: 10.1175/1520-0442(2000)013<2671:taortt>2.0.co;2
- 890 Dlugokencky, E. J., Nisbet, E. G., Fisher, R., and Lowry, D.: Global atmospheric methane: Budget,
891 changes and dangers, *Philosophical Transactions of the Royal Society A: Mathematical, Physical and
892 Engineering Sciences*, 369, 2058-2072, 2011. doi: 10.1098/rsta.2010.0341
- 893 Falk-Petersen, S., Hop, H., Budgell, W. P., Hegseth, E. N., Korsnes, R., Løyning, T. B., Børre Ørbæk, J.,
894 Kawamura, T., and Shirasawa, K.: Physical and ecological processes in the marginal ice zone of the
895 northern Barents Sea during the summer melt period, *Journal of Marine Systems*, 27, 131-159, 2000.
896 doi: 10.1016/S0924-7963(00)00064-6
- 897 Fer, I. and Drinkwater, K.: Mixing in the Barents Sea Polar Front near Hopen in spring, *Journal of Marine
898 Systems*, 130, 206-218, 2014. doi: 10.1016/j.jmarsys.2012.01.005
- 899 Fetterer, F., Knowles, K., Meier, W., Savoie, M., and Windnagel, A. K.: Sea Ice Index (version 3).
900 National Snow and Ice Data Center (NSDIC), Boulder, CO, 2017.
- 901 Gambacorta, A.: The NOAA Unique CrIS/ATMS Processing System (NUCAPS): Algorithm Theoretical
902 Basis Documentation, NOAA, NOAA Center for Weather and Climate Prediction, 78 pp., 2013.
903 http://www.ospo.noaa.gov/Products/atmosphere/soundings/nucaps/docs/NUCAPS_ATBD_20130821.pdf



- 904 Gammelsrød, T., Leikvin, Ø., Lien, V., Budgell, W. P., Loeng, H., and Maslowski, W.: Mass and heat
905 transports in the NE Barents Sea: Observations and models, *Journal of Marine Systems*. 75, 56-69,
906 2009. doi: 10.1016/j.marsys.2008.07.010
- 907 Gawarkiewicz, G. and Plueddemann, A. J.: Topographic control of thermohaline frontal structure in the
908 Barents Sea Polar Front on the south flank of Spitsbergen Bank, *Journal of Geophysical Research:*
909 *Oceans*, 100, 4509-4524, 1995. doi: 10.1029/94JC02427
- 910 Ghosh, A., Patra, P. K., Ishijima, K., Umezawa, T., Ito, A., Etheridge, D. M., Sugawara, S., Kawamura,
911 K., Miller, J. B., Dlugokencky, E. J., Krummel, P. B., Fraser, P. J., Steele, L. P., Langenfelds, R. L.,
912 Trudinger, C. M., White, J. W. C., Vaughn, B., Saeki, T., Aoki, S., and Nakazawa, T.: Variations in
913 global methane sources and sinks during 1910–2010, *Atmospheric Chemistry and Physics*, 15, 2595-
914 2612, 2015. doi: 10.5194/acp-15-2595-2015
- 915 Granskog, M. A., Macdonald, R. W., Mundy, C. J., and Barber, D. G.: Distribution, characteristics and
916 potential impacts of chromophoric dissolved organic matter (CDOM) in Hudson Strait and Hudson
917 Bay, Canada, *Continental Shelf Research*, 27, 2032-2050, 2007. doi: 10.1016/j.csr.2007.05.001
- 918 Graversen, R. G., Mauritsen, T., Tjernstrom, M., Kallen, E., and Svensson, G.: Vertical structure of recent
919 Arctic warming, *Nature*, 451, 53-56, 2008. doi: 10.1038/nature06502
- 920 Grebmeier, J. M., Bluhm, B. A., Cooper, L. W., Danielson, S. L., Arrigo, K. R., Blanchard, A. L., Clarke,
921 J. T., Day, R. H., Frey, K. E., Gradinger, R. R., Kędra, M., Konar, B., Kuletz, K. J., Lee, S. H.,
922 Lovvorn, J. R., Norcross, B. L., and Okkonen, S. R.: Ecosystem characteristics and processes
923 facilitating persistent macrobenthic biomass hotspots and associated benthivory in the Pacific Arctic,
924 *Progress in Oceanography*, 136, 92-114, 2015. doi: 10.1016/j.pocean.2015.05.006
- 925 Grebmeier, J. M., Overland, J. E., Moore, S. E., Farley, E. V., Carmack, E. C., Cooper, L. W., Frey, K.
926 E., Helle, J. H., McLaughlin, F. A., and McNutt, S. L.: A Major ecosystem shift in the Northern
927 Bering Sea, *Science*, 311, 1461-1464, 2006. doi: 10.1126/science.1121365
- 928 Gruber, N., Friedlingstein, P., Field, C., Valentini, R., Heimann, M., E Richey, J., Romero-Lankao, P.,
929 Ernst Detlef, S., and Chen, C.-T. A.: The vulnerability of the carbon cycle in the 21st century: An
930 assessment of carbon-climate-human interactions. In: *The Global Carbon Cycle*, Field, C. B. and
931 Raupach, M. R. (Eds.), Island Press, Washington D.C., 2004.
- 932 Harris, C. L., Plueddemann, A. J., and Gawarkiewicz, G. G.: Water mass distribution and polar front
933 structure in the western Barents Sea, *Journal of Geophysical Research: Oceans*, 103, 2905-2917,
934 1998. doi: 10.1029/97JC02790
- 935 Hoegh-Guldberg, O. and Bruno, J. F.: The impact of climate change on the world's marine ecosystems,
936 *Science*, 328, 1523-1528, 2010. doi: 10.1126/science.1189930
- 937 IASI-NG: <https://iasi-ng.cnes.fr/en/IASI-NG/index.htm>, last access: 1 June 2017 2017.
- 938 IPCC: Climate Change 2007: Synthesis Report. Contribution of Working Groups I, II, and III to the
939 Fourth Assessment Report of the Intergovernmental Panel on Climate Change, IPCC, Geneva,
940 Switzerland, 104 pp., 2007.
- 941 IPCC: Working Group 1 Contribution to the IPCC Fifth Assessment Report Climate Change 2013-The
942 Physical Science Basis, International Panel on Climate Change, IPCC Secretariat, Geneva,
943 Switzerland, 2216 pp., 2013.
- 944 Jakobsson, M., Mayer, L., Coakley, B., Dowdeswell, J. A., Forbes, S., Fridman, B., Hodnesdal, H.,
945 Noormets, R., Pedersen, R., Rebecco, M., Schenke, H. W., Zarayskaya, Y., Accettella, D., Armstrong,
946 A., Anderson, R. M., Bienhoff, P., Camerlenghi, A., Church, I., Edwards, M., Gardner, J. V., Hall, J.
947 K., Hell, B., Hestvik, O., Kristoffersen, Y., Marcussen, C., Mohammad, R., Mosher, D., Nghiem, S.
948 V., Pedrosa, M. T., Travaglini, P. G., and Weatherall, P.: The International Bathymetric Chart of the
949 Arctic Ocean (IBCAO) Version 3.0, *Geophysical Research Letters*, 39, L12609, 2012. doi:
950 10.1029/2012GL052219
- 951 James, R. H., Bousquet, P., Bussemann, I., Haeckel, M., Kipfer, R., Leifer, I., Ostrovsky, I., Niemann, H.,
952 Piskozub, J., Rehder, G., Treude, T., Vielstädte, L., and Greinert, J.: Effects of climate change on
953 methane emissions from seafloor sediments in the Arctic Ocean: A review, *Limnology and*
954 *Oceanography*, 61, 5281-5299, 2016. doi: 10.1002/lno.10307



- 955 John, J. G., Fiore, A. M., Naik, V., Horowitz, L. W., and Dunne, J. P.: Climate versus emission drivers of
956 methane lifetime against loss by tropospheric OH from 1860–2100, *Atmospheric Chemistry and*
957 *Physics*, 12, 12021–12036, 2012. doi: 10.5194/acp-12-12021-2012
- 958 Juahir, H., Zain, S. M., Aris, A. Z., Yusof, M. K., Samah, M. A. A., and Mokhtar, M. B.: Hydrological
959 trend analysis due to land use changes at Langat River Basin, *Environment Asia*, 3, 20–31, 2010.
960 <http://hdl.handle.net/10535/7032>
- 961 Judd, A. and Hovland, M.: *Seabed fluid flow: The impact on geology, biology and the marine*
962 *environment*, Cambridge University Press, Cambridge, UK, 2007.
- 963 Kahru, M., Brotas, V., Manzano-Sarabia, M., and Mitchell, B. G.: Are phytoplankton blooms occurring
964 earlier in the Arctic?, *Global Change Biology*, 17, 1733–1739, 2011. doi: 10.1111/j.1365-
965 2486.2010.02312.x
- 966 Kolstad, E. W.: A QuikSCAT climatology of ocean surface winds in the Nordic seas: Identification of
967 features and comparison with the NCEP/NCAR reanalysis, *Journal of Geophysical Research:*
968 *Atmospheres*, 113, D11106, 2008. doi: 10.1029/2007JD008918
- 969 Kort, E. A., Frankenberg, C., Miller, C. E., and Oda, T.: Space-based observations of megacity carbon
970 dioxide, *Geophysical Research Letters*, 39, L17806, 2012. doi: 10.1029/2012GL052738
- 971 Koyama, T., Stroeve, J., Cassano, J., and Crawford, A.: Sea ice loss and Arctic cyclone activity from
972 1979 to 2014, *Journal of Climate*, 30, 4735–4754, 2017. doi: 10.1175/jcli-d-16-0542.1
- 973 Kubryakov, A., Stanichny, S., and Zatsepin, A.: River plume dynamics in the Kara Sea from altimetry-
974 based lagrangian model, satellite salinity and chlorophyll data, *Remote Sensing of Environment*, 176,
975 177–187, 2016. doi: [10.1016/j.rse.2016.01.020](https://doi.org/10.1016/j.rse.2016.01.020)
- 976 Kuze, A., Suto, H., Nakajima, M., and Hamazaki, T.: Thermal and near infrared sensor for carbon
977 observation Fourier-transform spectrometer on the Greenhouse Gases Observing Satellite for
978 greenhouse gases monitoring, *Applied Optics*, 48, 6716–6733, 2009. doi: 10.1364/AO.48.006716
- 979 Leifer, I.: Characteristics and scaling of bubble plumes from marine hydrocarbon seepage in the Coal Oil
980 Point seep field, *Journal Geophysical Research*, 115, C11014, 2010. doi: 10.1029/2009JC005844
- 981 Leifer, I., Chernykh, D., Shakhova, N., and Semiletov, I.: Sonar gas flux estimation by bubble
982 insonification: Application to methane bubble flux from seep areas in the outer Laptev Sea, *The*
983 *Cryosphere*, 11, 1333–1350, 2017. doi: 10.5194/tc-11-1333-2017
- 984 Leifer, I., Jeuthe, H., Gjørund, S. H., and Johansen, V.: Engineered and natural marine seep, bubble-
985 driven buoyancy flows, *Journal of Physical Oceanography*, 39, 3071–3090, 2009. doi:
986 10.1175/2009JPO4135.1
- 987 Leifer, I. and MacDonald, I. R.: Dynamics of the gas flux from shallow gas hydrate deposits: Interaction
988 between oily hydrate bubbles and the oceanic environment, *Earth and Planetary Science Letters*, 210,
989 411–424, 2003. doi: 10.1016/S0012-821X(03)00173-0
- 990 Leifer, I. and Patro, R.: The bubble mechanism for methane transport from the shallow seabed to the
991 surface: A review and sensitivity study, *Continental Shelf Research*, 22, 2409–2428, 2002. doi:
992 10.1016/S0278-4343(02)00065-1
- 993 Leifer, I., Solomon, E., Schneider v. Deimling, J., Coffin, R., Rehder, G., and Linke, P.: The fate of
994 bubbles in a large, intense bubble plume for stratified and unstratified water: Numerical simulations
995 of 22/4b expedition field data, *Journal of Marine and Petroleum Geology*, 68B, 806–823, 2015. doi:
996 10.1016/j.marpetgeo.2015.07.025
- 997 Leifer, I., Tratt, D. M., Realmuto, V. J., Gerilowski, K., and Burrows, J. P.: Remote sensing atmospheric
998 trace gases with infrared imaging spectroscopy, *EOS, Transactions of the AGU*, 93, 525, 2012. doi:
999 10.1029/2012EO500006
- 1000 Li, S. and McClimans, T. A.: The effects of winds over a barotropic retrograde slope current, *Continental*
1001 *Shelf Research*, 18, 457–485, 1998. doi: [10.1016/S0278-4343\(97\)00077-0](https://doi.org/10.1016/S0278-4343(97)00077-0)
- 1002 Liang, Q., Chipperfield, M. P., Fleming, E. L., Abraham, N. L., Braesicke, P., Burkholder, J. B., Daniel,
1003 J. S., Dhomse, S., Fraser, P. J., Hardiman, S. C., Jackman, C. H., Kinnison, D. E., Krummel, P. B.,
1004 Montzka, S. A., Morgenstern, O., McCulloch, A., Mühle, J., Newman, P. A., Orkin, V. L., Pitari, G.,
1005 Prinn, R. G., Rigby, M., Rozanov, E., Stenke, A., Tummon, F., Velders, G. J. M., Visionsi, D., and



- 1006 Weiss, R. F.: Deriving global OH abundance and atmospheric lifetimes for long-lived gases: A search
1007 for CH₃CCl₃ alternatives, *Journal of Geophysical Research: Atmospheres*, 122, 11,914-911,933,
1008 2017. doi: 10.1002/2017JD026926
- 1009 Lien, V. S., Schlichtholz, P., Skagseth, Ø., and Vikebø, F. B.: Wind-driven Atlantic water flow as a direct
1010 mode for reduced Barents Sea ice cover, *Journal of Climate*, 30, 803-812, 2017. doi: 10.1175/jcli-d-
1011 16-0025.1
- 1012 Lien, V. S., Vikebø, F. B., and Skagseth, Ø.: One mechanism contributing to co-variability of the Atlantic
1013 inflow branches to the Arctic, *Nature Communications*, 4, 1488, 2013. doi: 10.1038/ncomms2505
- 1014 Loeng, H.: Features of the physical oceanographic conditions of the Barents Sea, *Polar Research*, 10, 5-
1015 18, 1991. doi: 10.1111/j.1751-8369.1991.tb00630.x
- 1016 MacDonald, I.: Remote sensing and sea-truth measurements of methane flux to the atmosphere
1017 (HYFLUX project), US Department of Energy, National Energy Technology Laboratory, 164 pp.,
1018 2011. <https://www.netl.doe.gov/research/oil-and-gas/project-summaries/methane-hydrate/de-nt0005638>
- 1019 MacDonald, I. R., Garcia-Pineda, O., Chanton, J., Kastner, M., Solomon, E., Leifer, I., Naehr, T., Yvon-
1020 Lewis, S., and John, K.: HYFLUX: Remote sensing and sea truth of CH₄ flux from the Gulf of
1021 Mexico seep system, Lake Baikal, Russia, 6-12 Sept. 2010 2010.
- 1022 Manabe, S. and Stouffer, R. J.: Sensitivity of a global climate model to an increase of CO₂ concentration
1023 in the atmosphere, *Journal of Geophysical Research: Oceans*, 85, 5529-5554, 1980. doi:
1024 10.1029/JC085iC10p05529
- 1025 Maslowski, W., Marble, D., Walczowski, W., Schauer, U., Clement, J. L., and Semtner, A. J.: On
1026 climatological mass, heat, and salt transports through the Barents Sea and Fram Strait from a pan-
1027 Arctic coupled ice-ocean model simulation, *Journal of Geophysical Research: Oceans*, 109, 2004. doi:
1028 10.1029/2001JC001039
- 1029 Mau, S., Römer, M., Torres, M. E., Bussmann, I., Pape, T., Damm, E., Geprägs, P., Wintersteller, P., Hsu,
1030 C. W., Loher, M., and Bohrmann, G.: Widespread methane seepage along the continental margin off
1031 Svalbard - from Bjørnøya to Kongsfjorden, *Scientific Reports*, 7, 42997, 2017. doi:
1032 10.1038/srep42997
- 1033 McClimans, T. A.: Entrainment/detrainment along river plumes. In: *Recent Research Advances in the*
1034 *Fluid Mechanics of Turbulent Jets and Plumes*, Davies, P. A. and Valente Neves, M. J. (Eds.),
1035 Kluwer Academic Publishers, Dordrecht, Germany, 1994.
- 1036 McClimans, T. A., Johannessen, B. O., and Nilsen, J. H.: Laboratory simulation of fronts between the
1037 various water masses in the Kara Sea, in *Oceanic Fronts and Related Phenomena (Konstantin Federov*
1038 *MEMorial Symposium)*, IOC Workshop Report No 159, 1999, 338-348.
- 1039 McClimans, T. A., Johnson, D. R., Krosshavn, M., King, S. E., Carroll, J., and Grenness, Ø.: Transport
1040 processes in the Kara Sea, *Journal of Geophysical Research: Oceans*, 105, 14121-14139, 2000. doi:
1041 10.1029/1999JC000012
- 1042 Moore, G. W. K.: The Novaya Zemlya Bora and its impact on Barents Sea air-sea interaction,
1043 *Geophysical Research Letters*, 40, 3462-3467, 2013. doi: 10.1002/grl.50641
- 1044 Myhre, C. L., Ferré, B., Platt, S. M., Silyakova, A., Hermansen, O., Allen, G., Pisso, I., Schmidbauer, N.,
1045 Stohl, A., Pitt, J., Jansson, P., Greinert, J., Percival, C., Fjaeraa, A. M., O'Shea, S. J., Gallagher, M.,
1046 Le Breton, M., Bower, K. N., Bauguitte, S. J. B., Dalsøren, S., Vadakkepuliambatta, S., Fisher, R.
1047 E., Nisbet, E. G., Lowry, D., Myhre, G., Pyle, J. A., Cain, M., and Mienert, J.: Extensive release of
1048 methane from Arctic seabed west of Svalbard during summer 2014 does not influence the
1049 atmosphere, *Geophysical Research Letters*, 43, 2016GL068999, 2016. doi: 10.1002/2016GL068999
- 1050 NASA: *Ocean Biology DAAC (OB.DAAC)*. 2015.
- 1051 Neukermans, G., Oziel, L., and Babin, M.: Increased intrusion of warming Atlantic water leads to rapid
1052 expansion of temperate phytoplankton in the Arctic, *Global Change Biology*, In Press, 2018. doi:
1053 10.1111/gcb.14075
- 1054 Nisbet, E. G., Dlugokencky, E. J., and Bousquet, P.: Methane on the rise—Again, *Science*, 343, 493-495,
1055 2014. doi: 10.1126/science.1247828



- 1056 NRC: The Arctic in the Anthropocene: Emerging Research Questions, The National Academies Press,
1057 Washington, DC, 2014.
- 1058 Onarheim, I. H. and Árrthun, M.: Toward an ice-free Barents Sea, *Geophysical Research Letters*, 44,
1059 8387-8395, 2017. doi: 10.1002/2017GL074304
- 1060 Önöz, B. and Bayazit, M.: The power of statistical tests for trend detection, *Turkish Journal of*
1061 *Engineering and Environmental Sciences*, 27, 247-251, 2003. doi,
1062 Overland, J. E. and Wang, M.: When will the summer Arctic be nearly sea ice free?, *Geophysical*
1063 *Research Letters*, 40, 2097-2101, 2013. doi: 10.1002/grl.50316
- 1064 Oziel, L., Sirven, J., and Gascard, J. C.: The Barents Sea frontal zones and water masses variability
1065 (1980–2011), *Ocean Science*, 12, 169-184, 2016. doi: 10.5194/os-12-169-2016
- 1066 Piechura, J. and Walczowski, W.: Warming of the West Spitsbergen current and sea ice North of
1067 Svalbard, *Oceanologia*, 51, 147-164, 2009. doi, [http://agro.icm.edu.pl/agro/element/bwmeta1.element.agro-](http://agro.icm.edu.pl/agro/element/bwmeta1.element.agro-article-fc388afa-b7bf-4387-8f5b-6285707fed8e)
1068 [article-fc388afa-b7bf-4387-8f5b-6285707fed8e](http://agro.icm.edu.pl/agro/element/bwmeta1.element.agro-article-fc388afa-b7bf-4387-8f5b-6285707fed8e)
- 1069 Polyak, L., Korsun, S., Febo, L. A., Stanovoy, V., Khusid, T., Hald, M., Paulsen, B. E., and Lubinski, D.
1070 J.: Benthic foraminiferal assemblages from the Souterhn Kara Sea - A river-influenced Arctic marine
1071 environment, *The Journal of Foraminiferal Research*, 32, 252-273, 2002. doi: 10.2113/32.3.252
- 1072 Prather, M. J., Holmes, C. D., and Hsu, J.: Reactive greenhouse gas scenarios: Systematic exploration of
1073 uncertainties and the role of atmospheric chemistry, *Geophysical Research Letters*, 39, L09803, 2012.
1074 doi: 10.1029/2012GL051440
- 1075 Rayner, P. J., Utembe, S. R., and Crowell, S.: Constraining regional greenhouse gas emissions using
1076 geostationary concentration measurements: a theoretical study, *Atmospheric Measurement*
1077 *Techniques*, 7, 3285-3293, 2014. doi: 10.5194/amt-7-3285-2014
- 1078 Razavi, A., Clerbaux, C., Wespes, C., Clarisse, L., Hurtmans, D., Payan, S., Camy-Peyret, C., and
1079 Coheur, P. F.: Characterization of methane retrievals from the IASI space-borne sounder,
1080 *Atmospheric Chemistry and Physics*, 9, 7889-7899, 2009. doi: 10.5194/acp-9-7889-2009
- 1081 Reeburgh, W. S.: Global methane biogeochemistry. In: *The Atmosphere. Treatise on Geochemistry*,
1082 Keeling, R. (Ed.), Elsevier-Pergamon, Oxford, 2003.
- 1083 Reeburgh, W. S.: Oceanic methane biogeochemistry, *Chemical Reviews*, 107, 486-513, 2007. doi:
1084 10.1021/cr050362v
- 1085 Rehder, G., Keir, R. S., Suess, E., and Rhein, M.: Methane in the Northern Atlantic controlled by
1086 microbial oxidation and atmospheric history, *Geophysical Research Letters*, 26, 587-590, 1999. doi:
1087 10.1029/1999GL900049
- 1088 Rehder, G., Leifer, I., Brewer, P. G., Friederich, G., and Peltzer, E. T.: Controls on methane bubble
1089 dissolution inside and outside the hydrate stability field from open ocean field experiments and
1090 numerical modeling, *Marine Chemistry*, 114, 19-30, 2009. doi: 10.1016/j.marchem.2009.03.004
- 1091 Rekeawicz, P.: <https://www.grida.no/resources/7482>) last access: January 2018 2018.
- 1092 Rigby, M., Montzka, S. A., Prinn, R. G., White, J. W. C., Young, D., O'Doherty, S., Lunt, M. F.,
1093 Ganesan, A. L., Manning, A. J., Simmonds, P. G., Salameh, P. K., Harth, C. M., Mühle, J., Weiss, R.
1094 F., Fraser, P. J., Steele, L. P., Krummel, P. B., McCulloch, A., and Park, S.: Role of atmospheric
1095 oxidation in recent methane growth, *Proceedings of the National Academy of Sciences*, 114, 5373-
1096 5377, 2017. doi: 10.1073/pnas.1616426114
- 1097 Saunio, M., Bousquet, P., Poulter, B., Peregón, A., Ciais, P., Canadell, J. G., Dlugokencky, E. J., Etiope,
1098 G., Bastviken, D., Houweling, S., Janssens-Maenhout, G., Tubiello, F. N., Castaldi, S., Jackson, R.
1099 B., Alexe, M., Arora, V. K., Beerling, D. J., Bergamaschi, P., Blake, D. R., Brailsford, G., Brovkin,
1100 V., Bruhwiler, L., Crevoisier, C., Crill, P., Curry, C., Frankenberg, C., Gedney, N., Höglund-
1101 Isaksson, L., Ishizawa, M., Ito, A., Joos, F., Kim, H. S., Kleinen, T., Krummel, P., Lamarque, J. F.,
1102 Langenfelds, R., Locatelli, R., Machida, T., Maksyutov, S., McDonald, K. C., Marshall, J., Melton, J.
1103 R., Morino, I., O'Doherty, S., Parmentier, F. J. W., Patra, P. K., Peng, C., Peng, S., Peters, G. P.,
1104 Pison, I., Prigent, C., Prinn, R., Ramonet, M., Riley, W. J., Saito, M., Schroeder, R., Simpson, I. J.,
1105 Spahni, R., Steele, P., Takizawa, A., Thornton, B. F., Tian, H., Tohjima, Y., Viovy, N., Voulgarakis,
1106 A., van Weele, M., van der Werf, G., Weiss, R., Wiedinmyer, C., Wilton, D. J., Wiltshire, A.,



- 1107 Worthy, D., Wunch, D. B., Xu, X., Yoshida, Y., Zhang, B., Zhang, Z., and Zhu, Q.: The global
1108 methane budget: 2000-2012, *Earth System Science Data Discussion*, 2016, 1-79, 2016. doi:
1109 10.5194/essd-2016-25
- 1110 Screen, J. A. and Simmonds, I.: The central role of diminishing sea ice in recent Arctic temperature
1111 amplification, *Nature*, 464, 1334-1337, 2010. doi: 10.1038/nature09051
- 1112 SEADAS: <https://seadas.gsfc.nasa.gov/help/>, last access: Jan 1 2016, <https://seadas.gsfc.nasa.gov/help/>, 2017.
- 1113 Sen, P. K.: Estimates of the regression coefficient based on Kendall's tau, *Journal of the American*
1114 *Statistical Association*, 63, 1379-1389, 1968. doi: 10.2307/2285891
- 1115 Shakhova, N., Semiletov, I., Gustafsson, O., Sergienko, V., Lobkovsky, L., Dudarev, O., Tumskey, V.,
1116 Grigoriev, M., Mazurov, A., Salyuk, A., Ananiev, R., Koshurnikov, A., Kosmach, D., Charkin, A.,
1117 Dmitrevsky, N., Karnaukh, V., Gunar, A., Meluzov, A., and Chernykh, D.: Current rates and
1118 mechanisms of subsea permafrost degradation in the East Siberian Arctic Shelf, *Nature*
1119 *Communications*, 8, 15872, 2017. doi: 10.1038/ncomms15872
- 1120 Shakhova, N., Semiletov Igor P., Leifer, I., Sergienko, V., Salyuk, A., Kosmach, D., Chernikh, D.,
1121 Stubbs, C., Nicolosky, D., Tumskey, V., Alexeev, V., and Gustafsson, O.: Ebullition and storm-
1122 induced methane release from the East Siberian Arctic Shelf, *Nature Geoscience*, 7, 64-70, 2013. doi:
1123 10.1038/ngeo2007
- 1124 Shakhova, N., Semiletov Igor P., Valentin Sergienko, Leopold Lobkovsky, Yusupov, V., Salyuk, A.,
1125 Salomatin, A., Chernykh, D., Kosmach, D., Panteleev, G., Joye, S., Charkin, A., Dudarev, O.,
1126 Meluzov, A., and Gustafsson, O.: The East Siberian Arctic Shelf: Towards further assessment of
1127 permafrost-related methane fluxes and role of sea ice, *Philosophical Transactions of the Royal*
1128 *Society A: Mathematical, Physical and Engineering Sciences*, 373, 1-13, 2015. doi:
1129 10.1098/rsta.2014.0451
- 1130 Skagseth, Ø., Furevik, T., Ingvaldsen, R., Loeng, H., Mork, K. A., Orvik, K. A., and Ozhigin, V.: Volume
1131 and heat transports to the Arctic Ocean via the Norwegian and Barents Seas. In: *Arctic-Subarctic*
1132 *Ocean Fluxes: Defining the Role of the Northern Seas in Climate*, Dickson, R. R., Meincke, J., and
1133 Rhines, P. (Eds.), Springer Netherlands, Dordrecht, 2008.
- 1134 Slagstad, D., Wassmann, P. F. J., and Ellingsen, I.: Physical constrains and productivity in the future
1135 Arctic Ocean, *Frontiers in Marine Science*, 2, 2015. doi: 10.3389/fmars.2015.00085
- 1136 Smedsrud, L. H., Esau, I., Ingvaldsen, R. B., Eldevik, T., Haugan, P. M., Li, C., Lien, V. S., Olsen, A.,
1137 Omar, A. M., Otterå, O. H., Risebrobakken, B., Sandø, A. B., Semenov, V. A., and Sorokina, S. A.:
1138 The role of the Barents Sea in the Arctic climate system, *Reviews of Geophysics*, 51, 415-449, 2013.
1139 doi: 10.1002/rog.20017
- 1140 Solomon, E., Kastner, M., MacDonald, I. R., and Leifer, I.: Considerable methane fluxes to the
1141 atmosphere from hydrocarbon seeps in the Gulf of Mexico, *Nature Geoscience*, 2, 561-565, 2009.
1142 doi: 10.1038/NGEO574
- 1143 Sonnemann, G. R. and Grygalashvily, M.: Global annual methane emission rate derived from its current
1144 atmospheric mixing ratio and estimated lifetime, *Annales Geophysicae*, 32, 277-283, 2014. doi:
1145 10.5194/angeo-32-277-2014
- 1146 Stedmon, C. A., Amon, R. M. W., Rinehart, A. J., and Walker, S. A.: The supply and characteristics of
1147 colored dissolved organic matter (CDOM) in the Arctic Ocean: Pan Arctic trends and differences,
1148 *Marine Chemistry*, 124, 108-118, 2011. doi: 10.1016/j.marchem.2010.12.007
- 1149 Stiansen, J. E., Korneev, O., Titov, O., Arneberg, P., Filin, A., Hansen, J. R., Høines, Å., and Marasaev,
1150 S.: Joint Norwegian-Russian Environmental Status 2008. Report on the Barents Sea Ecosystem. Part
1151 II – Complete Report, Norwegian Marine Data Center (NMDC)1502-8828, 375 pp., 2009.
1152 <https://www.barentsportal.com>
- 1153 Stroeve, J. C., Markus, T., Boisvert, L., Miller, J., and Barrett, A.: Changes in Arctic melt season and
1154 implications for sea ice loss, *Geophysical Research Letters*, 41, 1216-1225, 2014. doi:
1155 10.1002/2013GL058951
- 1156 Susskind, J., Barnett, C., Blaisdell, J., Iredell, L., Keita, F., Kouvaris, L., Molnar, G., and Chahine, M.:
1157 Accuracy of geophysical parameters derived from Atmospheric Infrared Sounder/Advanced



- 1158 Microwave Sounding Unit as a function of fractional cloud cover, *Journal of Geophysical Research:*
1159 *Atmospheres*, 111, D09S17, 2006. doi: 10.1029/2005JD006272
- 1160 Svendsen, H., Beszczynska-Møller, A., Hagen, J. O., Lefauconnier, B., Tverberg, V., Gerland, S., Ørbø, K.,
1161 J. B., Bischof, K., Papucci, C., Zajaczkowski, M., Azzolini, R., Bruland, O., Wiencke, C., Winther, J.
1162 G., and Dallmann, W.: The physical environment of Kongsfjorden–Krossfjorden, an Arctic fjord
1163 system in Svalbard, *Polar Research*, 21, 133-166, 2002. doi: 10.1111/j.1751-8369.2002.tb00072.x
- 1164 Tarnocai, C., Canadell, J. G., Schuur, E. A. G., Kuhry, P., Mazhitova, G., and Zimov, S.: Soil organic
1165 carbon pools in the northern circumpolar permafrost region, *Global Biogeochemical Cycles*, 23,
1166 GB2023, 2009. doi: 10.1029/2008gb003327
- 1167 Thonat, T., Saunio, M., Bousquet, P., Pison, I., Tan, Z., Zhuang, Q., Crill, P. M., Thornton, B. F.,
1168 Bastviken, D., Dlugokencky, E. J., Zimov, N., Laurila, T., Hatakka, J., Hermansen, O., and Worthy,
1169 D. E. J.: Detectability of Arctic methane sources at six sites performing continuous atmospheric
1170 measurements, *Atmospheric Chemistry and Physics*, 17, 8371-8394, 2017. doi: 10.5194/acp-17-
1171 8371-2017
- 1172 Timmermans, M.-L.: Sea Surface Temperature, NOAA, 106 pp., 2016. www.arctic.noaa.gov/Report-Card
- 1173 Tratt, D. M., Buckland, K. N., Hall, J. L., Johnson, P. D., Keim, E. R., Leifer, I., Westberg, K., and
1174 Young, S. J.: Airborne visualization and quantification of discrete methane sources in the
1175 environment, *Remote Sensing of Environment*, 154, 74-88, 2014. doi: 10.1016/j.rse.2014.08.011
- 1176 Turner, A. J., Jacob, D. J., Benmergui, J., Wofsy, S. C., Maasackers, J. D., Butz, A., Hasekamp, O., and
1177 Biraud, S. C.: A large increase in U.S. methane emissions over the past decade inferred from satellite
1178 data and surface observations, *Geophysical Research Letters*, 43, 2218-2224, 2016. doi:
1179 10.1002/2016GL067987
- 1180 Veefkind, J. P., Aben, I., McMullan, K., Förster, H., de Vries, J., Otter, G., Claas, J., Eskes, H. J., de
1181 Haan, J. F., Kleipool, Q., van Weele, M., Hasekamp, O., Hoogeveen, R., Landgraf, J., Snel, R., Tol,
1182 P., Ingmann, P., Voors, R., Kruizinga, B., Vink, R., Visser, H., and Levelt, P. F.: TROPOMI on the
1183 ESA Sentinel-5 Precursor: A GMES mission for global observations of the atmospheric composition
1184 for climate, air quality and ozone layer applications, *Remote Sensing of Environment*, 120, 70-83,
1185 2012. doi: 10.1016/j.rse.2011.09.027
- 1186 Vinje, T. and Kvambekk, Å. S.: Barents Sea drift ice characteristics, *Polar Research*, 10, 59-68, 1991. doi:
1187 10.3402/polar.v10i1.6728
- 1188 Voulgarakis, A., Naik, V., Lamarque, J. F., Shindell, D. T., Young, P. J., Prather, M. J., Wild, O., Field,
1189 R. D., Bergmann, D., Cameron-Smith, P., Cionni, I., Collins, W. J., Dalsøren, S. B., Doherty, R. M.,
1190 Eyring, V., Faluvegi, G., Folberth, G. A., Horowitz, L. W., Josse, B., MacKenzie, I. A., Nagashima,
1191 T., Plummer, D. A., Righi, M., Rumbold, S. T., Stevenson, D. S., Strode, S. A., Sudo, K., Szopa, S.,
1192 and Zeng, G.: Analysis of present day and future OH and methane lifetime in the ACCMIP
1193 simulations, *Atmospheric Chemistry Physics*, 13, 2563-2587, 2013. doi: 10.5194/acp-13-2563-2013
- 1194 Warzinski, R. P., Lynn, R., Hasljasmaa, I., Leifer, I., Shaffer, F., Anderson, B. J., and Levine, J. S.:
1195 Dynamic morphology of gas hydrate on a methane bubble in water: Observations and new insights
1196 for hydrate film models, *Geophysical Research Letters*, 41, 6841-6847, 2014. doi:
1197 10.1002/2014GL061665
- 1198 Westbrook, G. K., Chand, S., Rossi, G., Long, C., Bünz, S., Camerlenghi, A., Carcione, J. M., Dean, S.,
1199 Foucher, J. P., Flueh, E., Gei, D., Haacke, R. R., Madrussani, G., Mienert, J., Minshull, T. A., Nouzé,
1200 H., Peacock, S., Reston, T. J., Vanneste, M., and Zillmer, M.: Estimation of gas hydrate concentration
1201 from multi-component seismic data at sites on the continental margins of NW Svalbard and the
1202 Storegga region of Norway, *Marine and Petroleum Geology*, 25, 744-758, 2008. doi:
1203 10.1016/j.marpetgeo.2008.02.003
- 1204 Westbrook, G. K., Thatcher, K. E., Rohling, E. J., Piotrowski, A. M., Pälike, H., Osborne, A. H., Nisbet,
1205 E. G., Minshull, T. A., Lanoisellé, M., James, R. H., Hühnerbach, V., Green, D., Fisher, R. E.,
1206 Crocker, A. J., Chabert, A., Bolton, C., Beszczynska-Møller, A., Berndt, C., and Aquilina, A.: Escape
1207 of methane gas from the seabed along the West Spitsbergen continental margin, *Geophysical
1208 Research Letters*, 36, 2009. doi: 10.1029/2009gl039191



- 1209 Whitehead, J. A. and Salzig, J.: Rotating channel flow: Control and upstream currents, *Geophysical &*
1210 *Astrophysical Fluid Dynamics*, 95, 185-226, 2001. doi: 10.1080/03091920108203725
- 1211 Wofsy, S. C.: HIAPER Pole-to-Pole Observations (HIPPO): fine-grained, global-scale measurements of
1212 climatically important atmospheric gases and aerosols, *Philosophical Transactions of the Royal*
1213 *Society A: Mathematical, Physical and Engineering Sciences*, 369, 2073-2086, 2011. doi:
1214 10.1098/rsta.2010.0313
- 1215 Xiong, X., Barnet, C., Maddy, E. S., Gambacorta, A., King, T. S., and Wofsy, S. C.: Mid-upper
1216 tropospheric methane retrieval from IASI and its validation, *Atmospheric Measurement Techniques*,
1217 6, 2255-2265, 2013. doi: 10.5194/amt-6-2255-2013
- 1218 Xiong, X., Barnet, C. D., Zhuang, Q., Machida, T., Sweeney, C., and Patra, P. K.: Mid-upper tropospheric
1219 methane in the high Northern Hemisphere: Spaceborne observations by AIRS, aircraft measurements,
1220 and model simulations, *Journal of Geophysical Research: Atmospheres*, 115, D19309, 2010. doi:
1221 10.1029/2009jd013796
- 1222 Xiong, X., Han, Y., Liu, Q., and Weng, F.: Comparison of atmospheric methane retrievals from AIRS and
1223 IASI, *IEEE Journal of Selected Topics in Applied Earth Observations and Remote Sensing*, 9, 3297-
1224 3303, 2016. doi: 10.1109/JSTARS.2016.2588279
- 1225 Yamamoto-Kawai, M., McLaughlin, F. A., Carmack, E. C., Nishino, S., and Shimada, K.: Freshwater
1226 budget of the Canada Basin, Arctic Ocean, from salinity, $\delta^{18}\text{O}$, and nutrients, *Journal of*
1227 *Geophysical Research: Oceans*, 113, C01007, 2008. doi: 10.1029/2006JC003858
- 1228 Yurganov, L. and Leifer, I.: Estimates of methane emission rates from some Arctic and sub-Arctic areas
1229 based on orbital interferometer IASI data, *Current Problems in Remote Sensing of Earth from Space*
1230 *(Sovremennye Problemy Distsionnogo Zondirovaniya Zemli iz Kosmosa)*, 13, 173-183, 2016a.
1231 doi: 10.21046/2070-7401-2016-13-2-107-119
- 1232 Yurganov, L., Leifer, I., and Lund-Myhre, C.: Seasonal and interannual variability of atmospheric
1233 methane over Arctic Ocean from satellite data, *Current Problems in Remote Sensing of Earth from*
1234 *Space (Sovremennye Problemy Distsionnogo Zondirovaniya Zemli iz Kosmosa)*, 13, 107-119,
1235 2016. doi: 10.21046/2070-7401-2016-13-2-107-119
- 1236 Yurganov, L. N. and Leifer, I.: Abnormal concentrations of atmospheric methane over the Sea of Okhotsk
1237 during 2015/2016 winter, *Current Problems in Remote Sensing of Earth from Space (Sovremennye*
1238 *problemy distantsionnogo zondirovaniya zemli iz kosmosa)*, 1, 231-234, 2016b. doi: 10.21046/2070-
1239 7401-2016-13-3-231-234
- 1240
- 1241



1242 **TABLES**

1243 **Table 1.** Slopes of *SST* ($^{\circ}\text{C yr}^{-1}$), CH_4 (ppb yr^{-1}), and CH_4' (ppb yr^{-1}) for focus boxes. ^a

1244	Box	<i>SST</i>	CH_4	CH_4	CH_4' (Barents) ^b	CH_4' (Arctic) ^c
1245		2003-2015	2003-2015	2003-2015	2005-2015	2003-2015
1246	A1	0.102	3.35	3.26	0.179	0.0750
1247	A2	0.0319	3.49	3.38	0.267	0.213
1248	A3	0.00178	3.19	3.17	-0.0185	0.00574
1249	A4	0.0867	3.37	3.60	0.310	0.391
1250	A5	0.0279	3.10	3.22	0.0105	0.0319
1251	A6	0.00259	3.07	3.24	-0.0123	0.0548
1252	A7	0.0323	3.06	3.27	-0.0460	-0.119
1253	A8	0.0552	3.11	3.35	0.0642	-0.0544
1254	A9	0.145	3.20	3.44	0.103	0.109
1255	A100	0.0527	3.32	3.51	0.122	0.0613

1256 ^a *SST* – Sea Surface Temperature, CH_4' – methane anomaly.

1257 ^b CH_4' relative to the Barents Sea

1258 ^c CH_4' relative to the Arctic Ocean

1259 **FIGURE CAPTIONS**

1260 **Figure 1 a)** Arctic and sub-arctic methane (CH_4), 0.5° gridded, 0-4 km altitude, 2016, from the Infrared
1261 Atmospheric Sounding Interferometer (IASI); mountainous regions blanked. Data were filtered as in
1262 Yurganov and Leifer (2016a). Data key on panel.

1263 **Figure 2 a)** Map of the Arctic Ocean, showing study area (Blue Square) and average January and
1264 September 2003-2015 ice extent. **b)** Bathymetry of the study area (87.468 N, 1.219E; 72.056N, 0.173E;
1265 63.008N, 48.05E; 69.707N, 82.793E) from Jakobsson et al. (2012). Dashed line shows approximate
1266 Barents Sea boundaries. Star shows scoping study pixels location. Depth data key on panel.

1267 **Figure 3.** Comparison of the sea surface temperature (*SST*) and methane (CH_4) for 2003-2015 for pixels
1268 between Franz Josef Land and Novaya Zemlya (**Fig. 2b, Star, Supp. Table 1, Box A2**). Red diamonds
1269 show *SST* and CH_4 averages within the study area. Blue and green ovals highlight pixels with different
1270 CH_4 trends for *SST* (all CH_4), and ($\text{CH}_4 > 1925$ ppb), respectively.

1271 **Figure 4. a)** Currents for Barents and nearby seas, bathymetry features, and focus-area locations. Green,
1272 red, and blue arrows are coastal, warm Atlantic origin, and cold polar currents, respectively. Broken lines
1273 illustrate current subduction. Bathymetry from Jakobsson et al. (2012). **b)** Monthly ice extent for 2015.
1274 Focus study boxes (numbered); coordinates listed in **Supp. Table S1**.

1275 **Figure 5. a)** Surface in situ methane (CH_4) during northward Barents Sea transect on the *R/V Akademik*
1276 *Federov* for 21 Aug. 2013. Also shown is the 300-m depth contour and edges of the Murman Coastal
1277 Current, from pinru(http://www.pinru.ru/labs/hid/kolsec1_e.htm). Data key on figure. **b)** CH_4 profiles
1278 during northerly and southerly transits, labeled.

1279 **Figure 6.** Ice-free months from 2003 to 2015 for focus boxes for **a)** Northern Barents (A1-A3), **b)**
1280 Northwest of Barents (A4-A6), and **c)** Southern Barents (A7-A10). Box names on panels. See **Fig. 3c** and
1281 **Supp. Table S1** for locations.

1282 **Figure 7.** Sea surface temperature (*SST*) time series for 2003 to 2015 for focus box areas **a)** Northern
1283 Barents (A1-A3), **b)** Northwest of Barents (A4-A6), and **c)** Southern Barents (A7-A10). Annual values
1284 are average of all months, generally May-October, which are ice-free. Box names on panel a. Data key on
1285 figure.

1286 **Figure 8.** Focus study area methane (CH_4) trends, 2003 to 2015 for **a)** Arctic Ocean study boxes, **b)**
1287 Northwest of Barents study boxes, and **c)** Barents Sea focus study boxes. Annual data and 3 year, rolling-
1288 average data shown. Anomaly is relative to entire Barents Sea. Data key on figure.

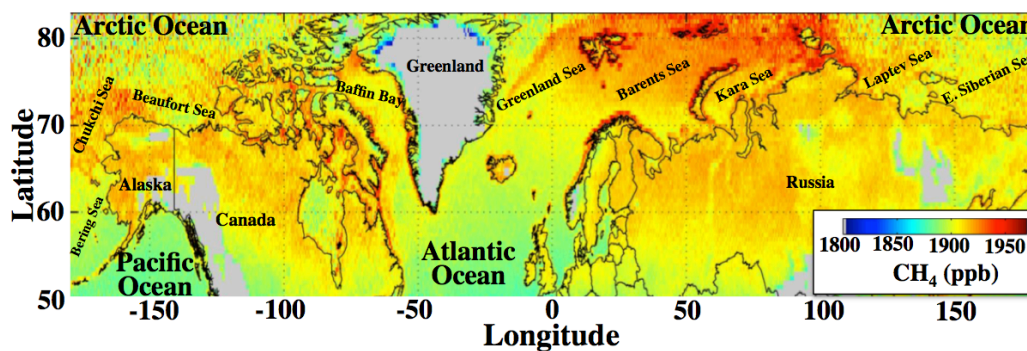
1289 **Figure 9.** Trends for focus area A8 (north of Murman) for 2003 to 2015 for CH_4 and *SST*. Data key on
1290 figure.

1291 **Figure 10.** Mean values for 2003 to 2015 of sea surface temperature (*SST*) for **a)** June and **b)** September.
1292 Mean methane (CH_4) concentration for **c)** June and **d)** September. Median ice edge for same period is
1293 shown. Years with reduced ice extent contribute to values of *SST* north of this ice edge. Data key on
1294 figure.

1295 **Figure 11.** Linear trends for 2003 to 2015 of sea surface temperature ($dSST/dt$) for **a)** June and **b)**
1296 September. Methane concentration trend ($d\text{CH}_4/dt$) for **c)** June and **d)** September. ND – not detectable –
1297 failed statistical test. Blue, black dashed lines shows 100 and 50 m contour, respectively. Data key on
1298 figure.

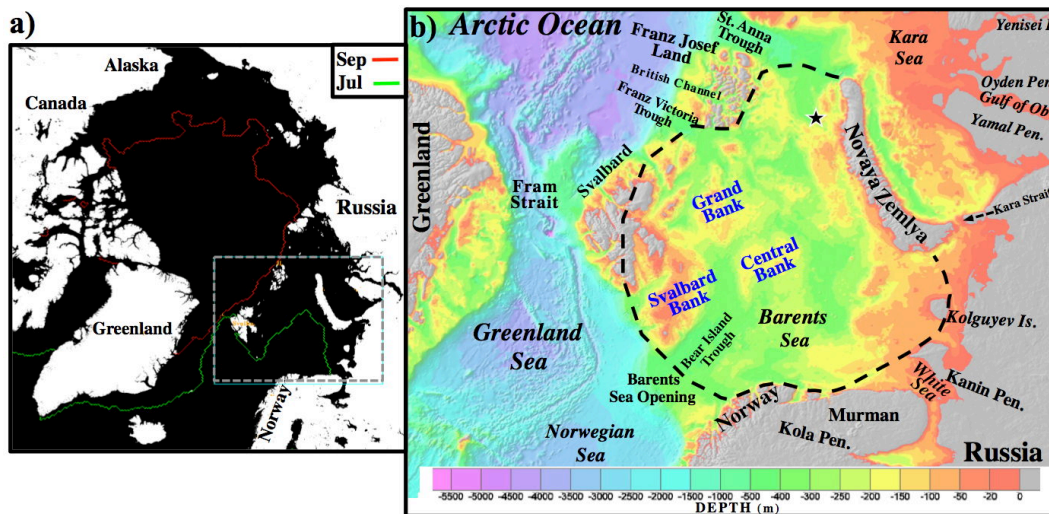


1299 FIGURES



1300
1301 **Figure 1** Arctic and sub-arctic methane (CH_4), 0.5° gridded, 0-4 km altitude, 2016, from the Infrared
1302 Atmospheric Sounding Interferometer (IASI); mountainous regions blanked. Data were filtered as in
1303 Yurganov and Leifer (2016a). Data key on panel.

1304



1305

1306

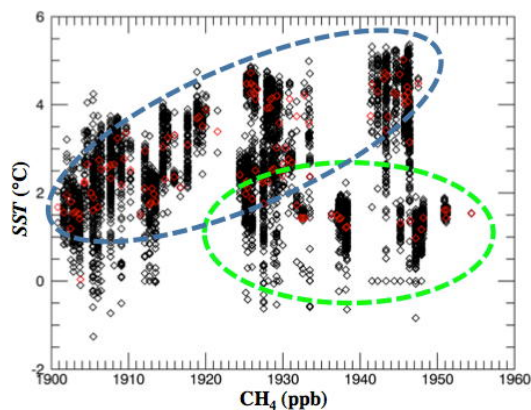
1307

1308

1309

1310

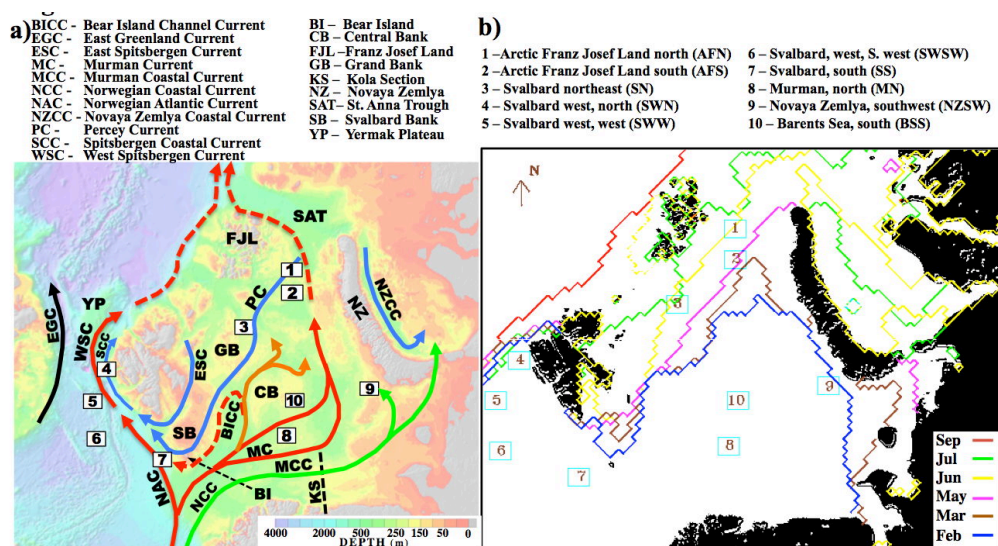
Figure 2 a) Map of the Arctic Ocean, showing study area (Blue Square) and average January and September 2003-2015 ice extent. b) Bathymetry of the study area (87.468 N, 1.219E; 72.056N, 0.173E; 63.008N, 48.05E; 69.707N, 82.793E) from Jakobsson et al. (2012). Dashed line shows approximate Barents Sea boundaries. Star shows scoping study pixels location. Depth data key on panel.



1311

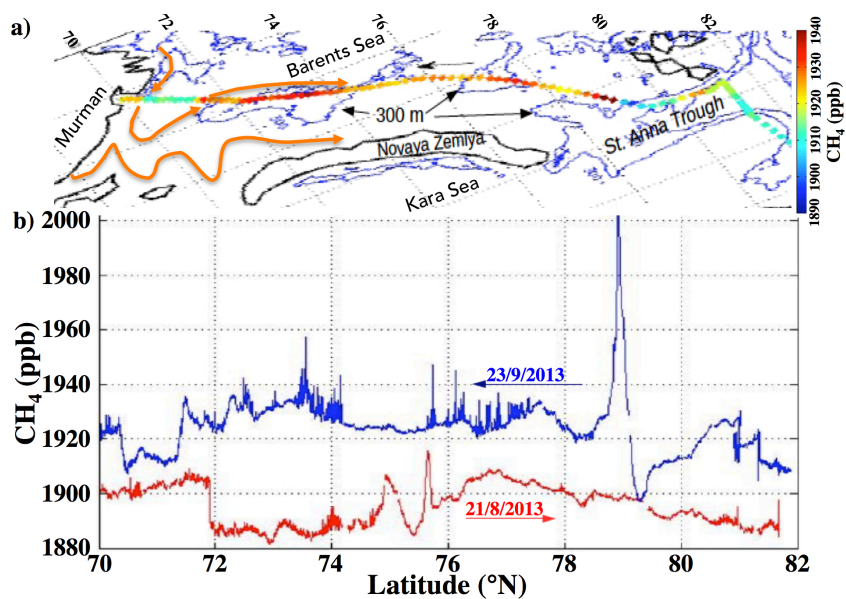
1312 **Figure 3.** Comparison of the sea surface temperature (*SST*) and methane (CH_4) for 2003-2015 for pixels
1313 between Franz Josef Land and Novaya Zemlya (**Fig. 2b, Star, Supp. Table 1, Box A2**). Red diamonds
1314 show *SST* and CH_4 averages within the study area. Blue and green ovals highlight pixels with different
1315 CH_4 trends for *SST* (all CH_4), and ($\text{CH}_4 > 1925$ ppb), respectively.

1316



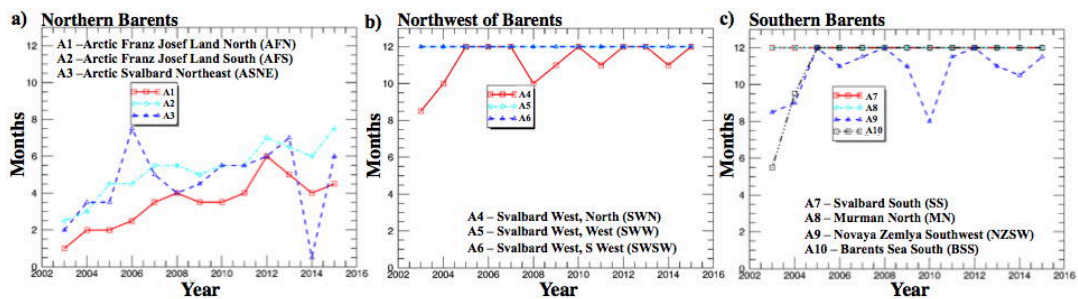
1317
 1318 **Figure 4.** a) Currents for Barents and nearby seas, bathymetry features, and focus-area locations. Green,
 1319 red, and blue arrows are coastal, warm Atlantic origin, and cold polar currents, respectively. Broken lines
 1320 illustrate current subduction. Bathymetry from Jakobsson et al. (2012). b) Monthly ice extent for 2015.
 1321 Focus study boxes (numbered); coordinates listed in **Supp. Table S1**.

1322



1323
1324
1325
1326
1327
1328

Figure 5. a) Surface in situ methane (CH_4) during northward Barents Sea transect on the *R/V Akademik Fyodorov* for 21 Aug. 2013. Also shown is the 300-m depth contour and edges of the Murman Coastal Current, from PINRU (http://www.pinro.ru/labs/hid/kolsec1_e.htm). Data key on figure. b) CH_4 profiles during northerly and southerly transits, labeled.



1329

1330

1331

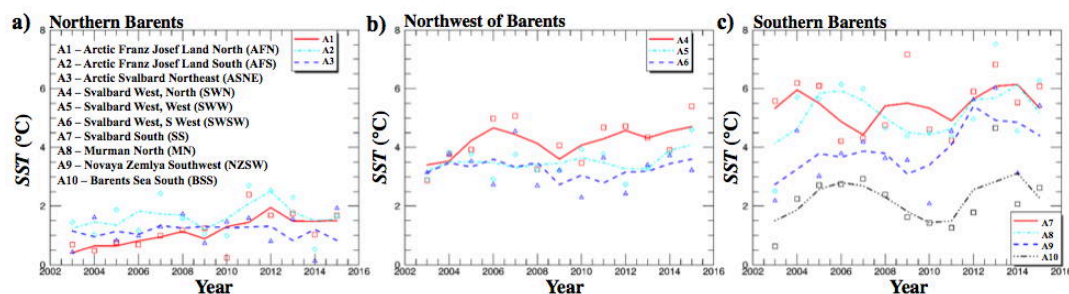
1332

1333

Figure 6. Ice-free months from 2003 to 2015 for focus boxes for **a)** Northern Barents (A1-A3), **b)** Northwest of Barents (A4-A6), and **c)** Southern Barents (A7-A10). Box names on panels. See **Fig. 3c** and **Supp. Table S1** for locations.



1334



1335

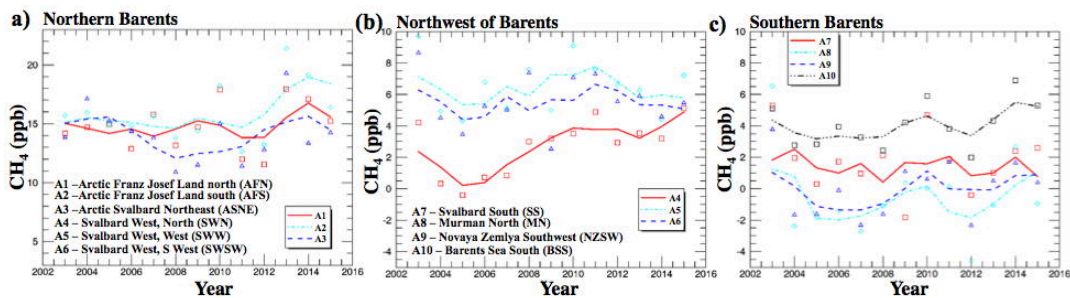
1336

1337

1338

1339

Figure 7. Sea surface temperature (*SST*) time series for 2003 to 2015 for focus box areas **a)** Northern Barents (A1-A3), **b)** Northwest of Barents (A4-A6), and **c)** Southern Barents (A7-A10). Annual values are average of all months, generally May-October, which are ice-free. Box names on panel a. Data key on figure.



1340

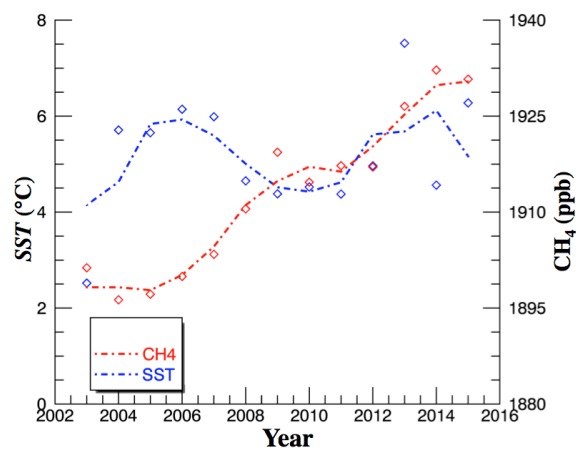
1341

1342

1343

1344

Figure 8. Focus study area methane (CH₄) trends, 2003 to 2015 for **a)** Arctic Ocean study boxes, **b)** Northwest of Barents study boxes, and **c)** Barents Sea focus study boxes. Annual data and 3 year, rolling-average data shown. Anomaly is relative to entire Barents Sea. Data key on figure.



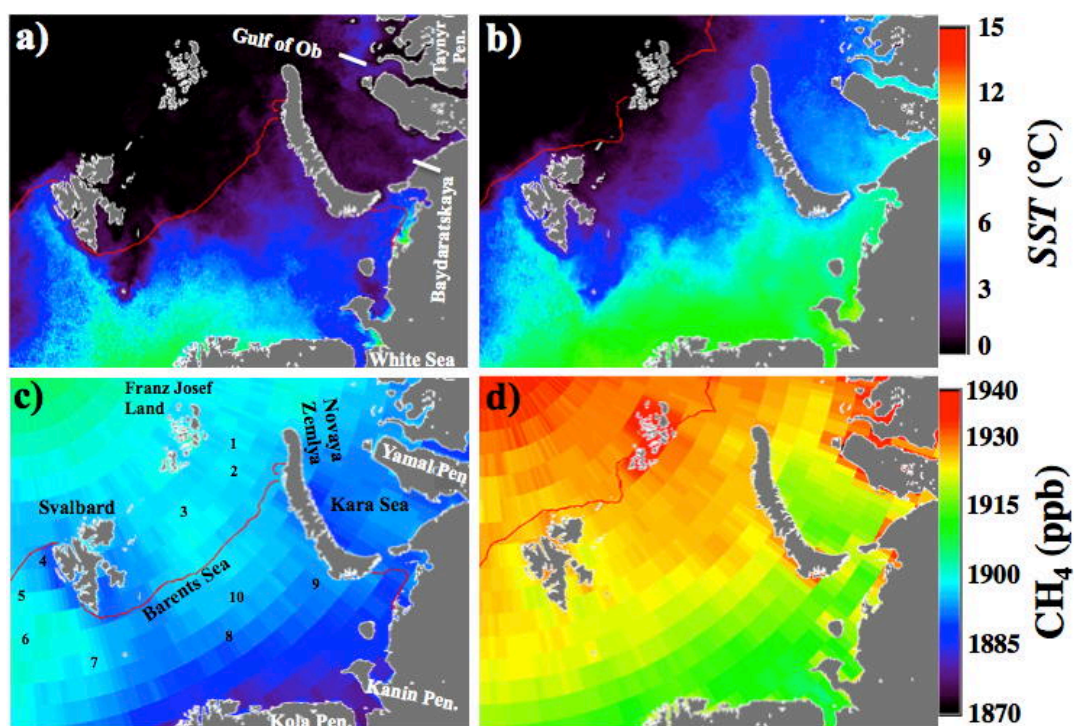
1345

1346 **Figure 9.** Trends for focus area A8 (north of Murman) for 2003 to 2015 for CH₄' and SST. Data key on
1347 figure.

1348

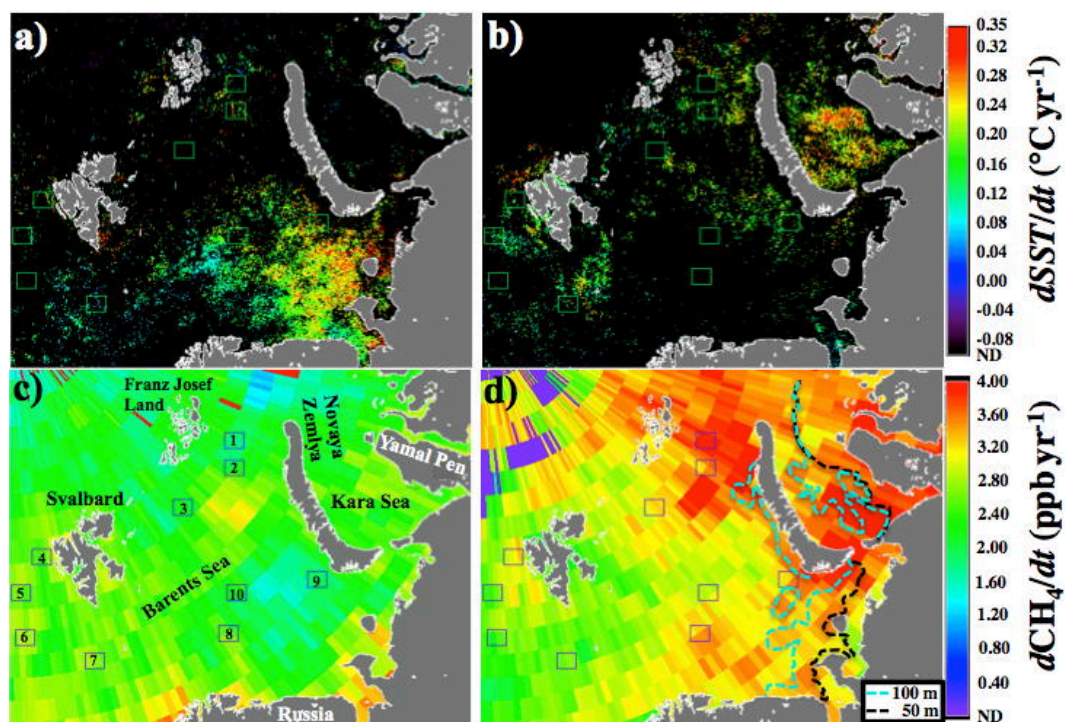


1349



1350
1351
1352
1353
1354

Figure 10. Mean values for 2003 to 2015 of sea surface temperature (*SST*) for **a)** June and **b)** September. Mean methane (CH_4) concentration for **c)** June and **d)** September. Median ice edge for same period is shown. Years with reduced ice extent contribute to values of *SST* north of this ice edge. Data key on figure.



1355
1356
1357
1358
1359

Figure 11. Linear trends for 2003 to 2015 of sea surface temperature ($dSST/dt$) for **a)** June and **b)** September. Methane concentration trend (dCH_4/dt) for **c)** June and **d)** September. ND – not detectable – failed statistical test. Blue, black dashed lines shows 100 and 50 m contour, respectively. Data key on figure.